https://doi.org/10.5194/essd-2026-593
Preprint. Discussion started: 4 September 2026

Open Access Earth System Science Data Discussions

Airborne measurements from the Southern California Investigation of Low cloud and Land Aerosol (SCILLA)

Mikael K. Witte[1], Roya Bahreini[2], Sierra Bollinger[1], Anthony Bucholtz[1], Patrick Y. Chuang[3], Don Collins[2], Minghao Han[2], Mason D. Leandro[3,6], Alexander B. MacDonald[2], Andrew R. Metcalf[4], Bradley Ries[2], Nimya Sunil[5], Dongli Wang[4], and Lisa R. Welp[5]

[1]Naval Postgraduate School, Monterey, CA
[2]University of California Riverside, Riverside, CA
[3]University of California Santa Cruz, Santa Cruz, CA
[4]Clemson University, Clemson, SC
[5]Purdue University, West Lafayette, IN
[6]Artium Technologies, Inc., Sunnyvale, CA

Correspondence: Mikael K. Witte (mikael.witte@nps.edu)

Abstract. The Southern California Investigation of Low cloud and Land Aerosol (SCILLA) was an airborne field experiment flown in June 2023 based out of San Diego, California. The objectives of the experiment were to investigate dynamical controls on aerosol transport from land over the ocean, quantify the impacts of aerosol-cloud interactions on planetary boundary layer (PBL) evolution, and characterize gradients in atmospheric properties across the PBL-topping inversion to constrain transport hypotheses. A total of 20 research flights were flown over the Southern California Bight, with 18 flights in the vicinity of San Clemente Island and an additional 2 flights over the Los Angeles basin and offshore of the adjacent coastline near Santa Monica and Malibu. A twin turboprop aircraft was outfitted with a broad array of instruments to sample basic meteorology (thermodynamics and winds); aerosol physical, chemical and radiative properties; cloud and drizzle microphysics; radiation; and trace gases. Detailed descriptions of flight sampling strategies, aircraft instrumentation and derived products are given and an overview of each research flight is provided as a reference for data users. The primary dataset, merged 1 and 10 Hz aircraft data, is globally available at https://doi.org/10.5281/zenodo.21826965.

1 Introduction

The Southern California Bight is a region characterized by complicated atmospheric dynamics and significant impacts on air quality from human activities both offshore (e.g., from ships transiting to/from the Port of Long Beach) and onshore (e.g., emissions from the heavily populated Southern California region). During the late spring and early summer months, shallow mesoscale eddies associated with persistent and widespread low cloud coverage have been shown to correlate with improved air quality in the Los Angeles Basin (Wakimoto, 1987) but may also be associated with enhanced offshore transport of continental pollutants over nearshore waters as demonstrated by satellite retrievals of cloud drop number concentration N_d in Figure 1. The Southern California Investigation of Low cloud and Land Aerosol (SCILLA) was conducted over the Southern California Bight (henceforth referred to as “the Bight”) in June 2023 to provide aircraft in situ measurements of aerosol, cloud, trace

https://doi.org/10.5194/essd-2026-593
Preprint. Discussion started: 4 September 2026

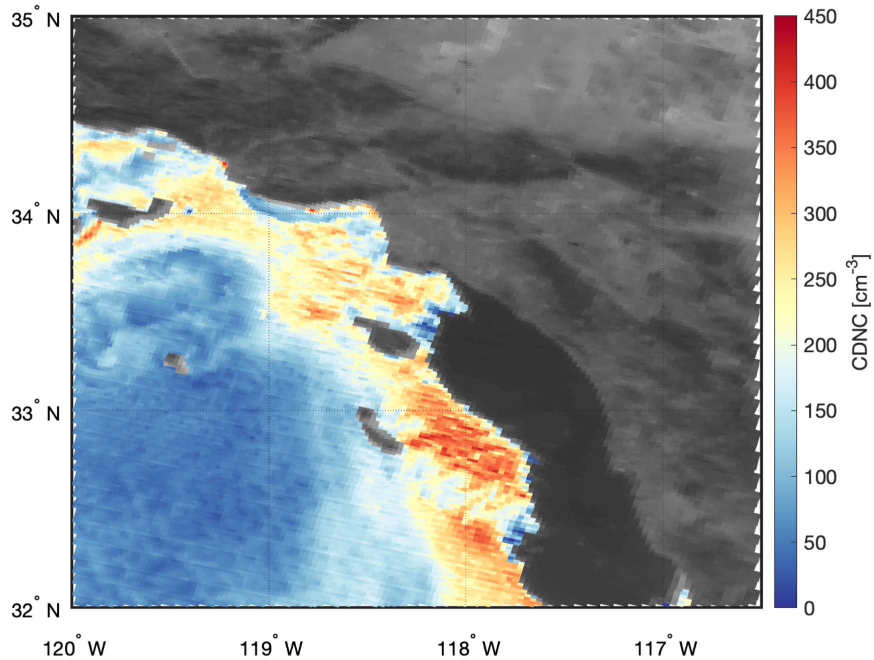

Figure 1. Visible imagery (band 1, 0.645 μm) from Terra MODIS with retrieved cloud drop number concentration (CDNC) overlaid (only retrievals over ocean surface are shown). Image taken 30 June 2023 1850 UTC.

gas, turbulence, and thermodynamic properties. These measurements will be used to evaluate process-oriented hypotheses regarding aerosol-cloud interactions, multi-scale dynamics, and offshore transport pathways for continental particulate in the near-coastal environment. The acronym for the experiment was inspired by Scylla, a sea monster in Greek mythology who preyed on passing ships attempting to avoid Charybdis, a treacherous eddy/whirlpool.

2 Overview of flight activities

2.1 Aircraft and general approach

SCILLA research flights were flown by the Naval Postgraduate School (NPS) Center for Interdisciplinary Remotely Piloted Aircraft Studies (CIRPAS) Twin Otter, a twin turboprop aircraft ideally suited for boundary layer sampling due to its maneuverability and relatively slow airspeed. The Twin Otter was based at Montgomery Field, San Diego, California for the duration of the campaign and a total of 21 research flights (RFs) were conducted between 5-30 June 2023. The first mission (RF01) was a post-ferry shakedown flight; there was little usable data from this flight and it is not discussed in the remainder of the paper. Of the remaining 20 flights, most (18 of 20) sampled the planetary boundary layer (PBL) and lower free troposphere in the

https://doi.org/10.5194/essd-2026-593
Preprint. Discussion started: 4 September 2026

vicinity of San Clemente Island (SCI; 32.9029° N, 118.4981° W), the southernmost of the Channel Islands. An additional two research flights (RFs 09 and 11) were flown over the Los Angeles Basin and adjacent coastline to characterize aerosol chemical composition and physical properties in continental outflow from the LA basin. Figure 2 shows examples of this dynamical regime with early morning offshore flow from the LA basin out over the Bight.

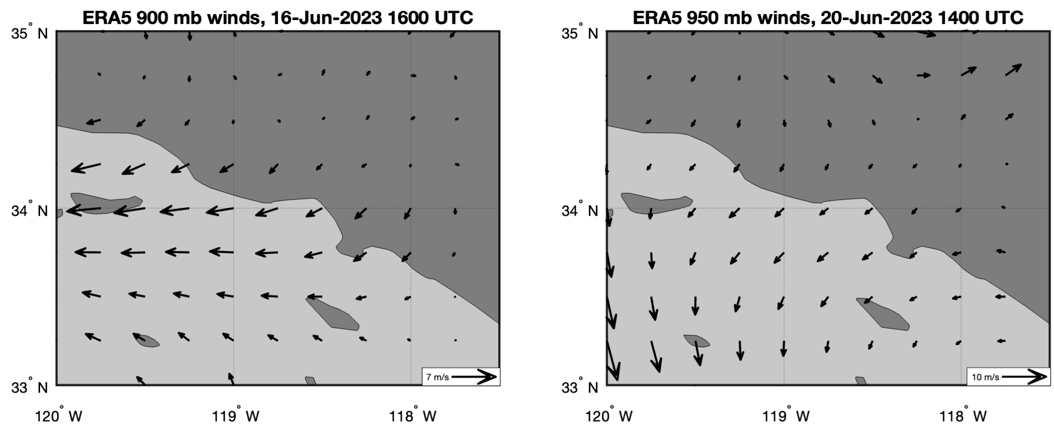

Figure 2. Examples of offshore flow over the Southern California Bight from the LA basin preceding aerosol flights RF09 (left) and RF11 (right).

SCI was the reference landmark for reasons both scientific and pragmatic. From a scientific perspective, satellite retrievals (as in Fig. 1) show that there is often a pronounced gradient in cloud microphysical properties near SCI and its neighbor to the north, Santa Catalina Island. Understanding how such gradients form and are maintained was of keen interest. From an operational perspective, airspace restrictions close to shore, near Channel Islands National Park and Marine Sanctuary, and in the vicinity of the Los Angeles International Airport approach/takeoff lanes placed strict limitations on where in-cloud sampling was feasible. With the exception of the two "LA outflow" flights (RFs 09 and 11), daily flight plans were determined based on the availability of military airspace in warning area 291-E in coordination with the Fleet Area Control and Surveillance Facility, San Diego (military-operated authority for air traffic in the region). There was significant day-to-day variability in which segments of the warning area were available for research flights, and this is reflected in the range of horizontal sampling strategies adopted over the course of the campaign (see Fig. 3 and the following section).

2.2 Sampling strategies

Research flights are divided into five categories based on the scientific purpose and aircraft sampling strategy employed (Fig. 3 and Table 1): aerosol characterization (denoted "Aerosol" in Table 1; RFs 09, 11, 13, 20); clean/wake contrast characterization ("Contrast"; i.e., one module upwind of SCI, one or more modules downwind; RFs 02, 04, 15, 16, 18, 19, 21); cloudy boundary layer (BL) characterization upwind of SCI ("Upwind"; RFs 07, 14); downwind island wake/BL characterization ("Downwind"; RFs 03, 08, 12, 17); and wake edge gradient characterization ("Wake edge"; RFs 05, 06, 10). In all cases, horizontal sampling

https://doi.org/10.5194/essd-2026-593
Preprint. Discussion started: 4 September 2026

Flight no.	Date	Time (UTC)	Flight type
RF01	5 June 2023	22:32-01:01*	Shakedown
RF02	6 June 2023	15:34-19:56	Contrast
RF03	9 June 2023	14:29-19:19	Downwind
RF04	10 June 2023	14:27-18:57	Contrast
RF05	11 June 2023	14:27-19:09	Wake edge
RF06	12 June 2023	14:32-19:14	Wake edge
RF07	13 June 2023	14:30-19:04	Upwind
RF08	15 June 2023	14:30-19:07	Downwind
RF09	16 June 2023	14:42-19:44	Aerosol
RF10	19 June 2023	14:25-18:29	Wake edge
RF11	20 June 2023	14:21-19:01	Aerosol
RF12	21 June 2023	14:25-18:08	Aerosol
RF13	22 June 2023	14:35-18:33	Downwind
RF14	23 June 2023	14:23-18:35	Upwind
RF15	24 June 2023	14:23-18:43	Contrast
RF16	26 June 2023	14:22-19:04	Contrast
RF17	27 June 2023	14:27-18:58	Downwind
RF18	28 June 2023	14:38-19:04	Contrast
RF19	29 June 2023	14:26-19:12	Contrast
RF20	29 June 2023	19:44-22:21	Aerosol
RF21	30 June 2023	14:20-19:14	Contrast

Table 1. Basic information on SCILLA research flights. Asterisk in the Time column of RF01 indicates that the flight ended the next day UTC (6 June 2023). A more detailed description of flight types can be found in the text.

was Eulerian in nature, i.e., modules were flown between fixed waypoints such that no spatial/temporal correlations should be inferred between subsequent modules. The sampling strategy for each flight was chosen based on environmental conditions (cloudy vs. clear over the Bight) and airspace availability. Flights were generally scheduled shortly after sunrise (takeoff 0700-0730 local time) to facilitate cloud sampling before daily cloud burnoff/offshore retreat. Finally, different vertical sampling strategies were used in coupled vs. decoupled cloudy boundary layers and clear-air conditions as described in detail below.

2.2.1 Vertical sampling for aerosol characterization

Vertical sampling during aerosol characterization flights consisted of two primary strategies: missed approaches to Los Angeles area airports (Long Beach Airport, LGB; Santa Monica Airport, SMO; Torrance Airport, TOA) to sample vertical variability

https://doi.org/10.5194/essd-2026-593
Preprint. Discussion started: 4 September 2026

Open Access Earth System Science Data Discussions

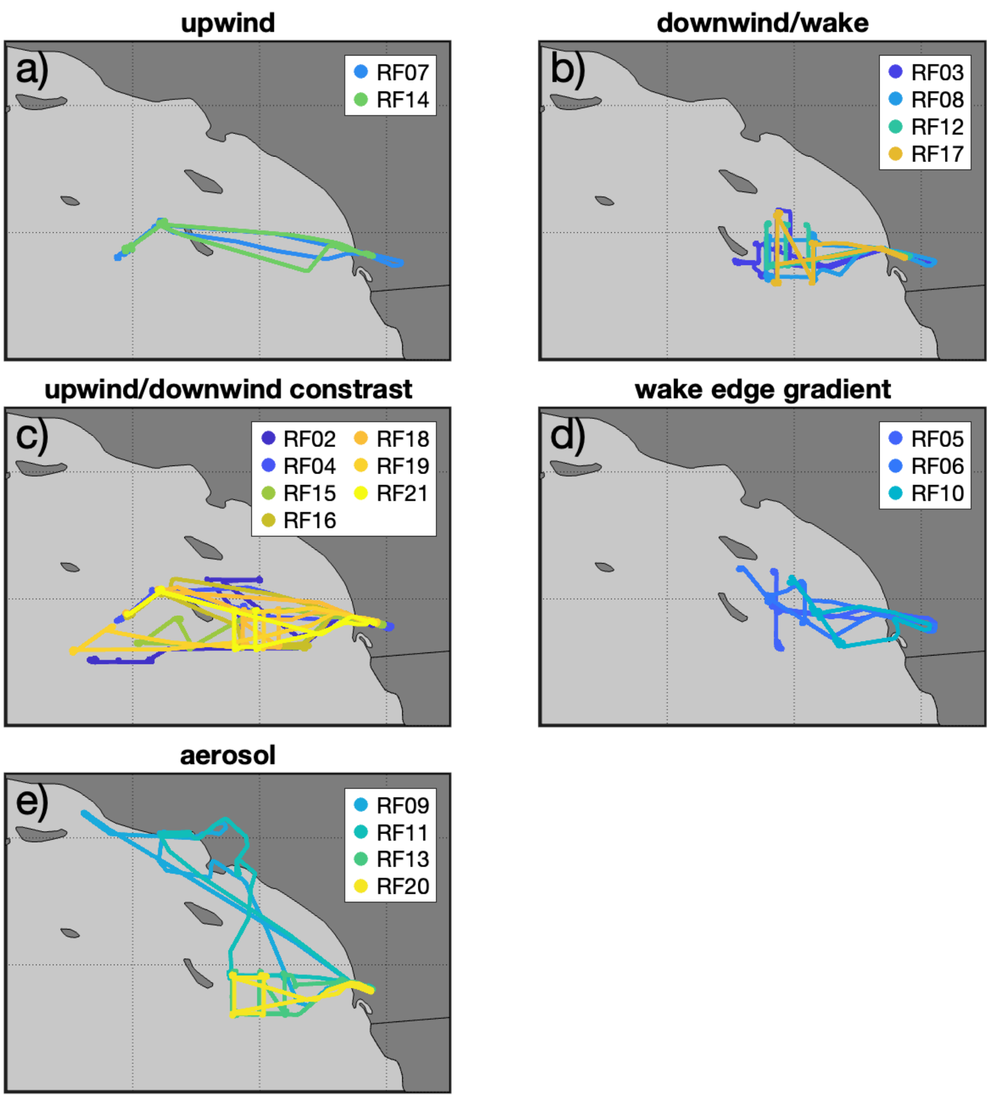

Figure 3. SCILLA flight tracks grouped by horizontal sampling strategy. RF01 is omitted as it was not a science-oriented flight.

in the urban environment and repeated level legs along a consistent line at multiple altitudes in the lower free troposphere (informally known as "racetracks") offshore of the Malibu area to sample outflow from the Los Angeles basin.

2.2.2 Vertical sampling in coupled vs. decoupled cloudy boundary layers

The primary considerations for vertical sampling of the cloudy boundary layer were to (1) constrain vertical flux terms in the cloud condensation nuclei (CCN) budget and (2) characterize vertical cloud structure. Figure 4 shows two examples from SCILLA flights: one in a cloud-topped, surface-coupled planetary boundary layer (PBL; panel a) and the other in a cloud-

https://doi.org/10.5194/essd-2026-593
Preprint. Discussion started: 4 September 2026

Open Access Earth System Science Data Discussions

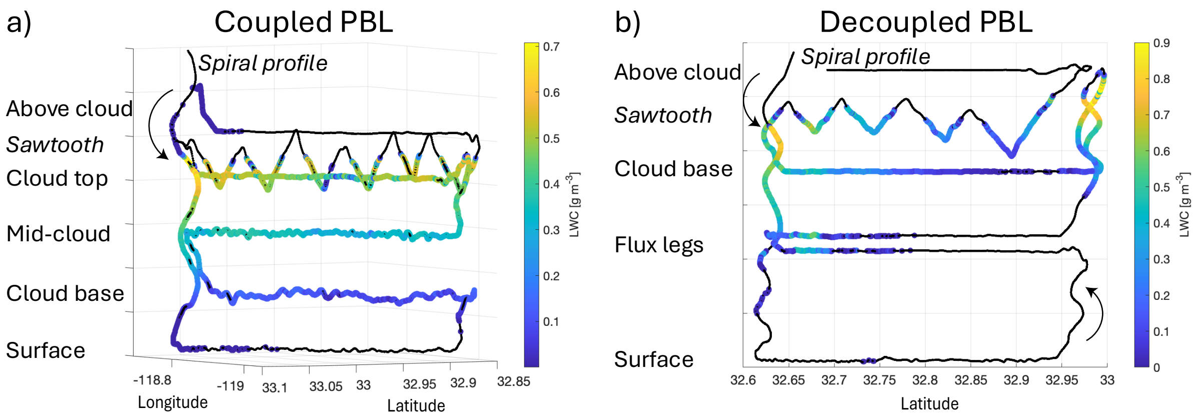

Figure 4. Examples of vertical sampling. The flight track is shown in black with nonzero liquid water content (LWC) overlaid where applicable. Annotation shows leg names. Most legs were flown level; annotation in italics denotes segments flown at variable altitude and the curving arrows denote downward spirals. Panel a: a typical module flown in the cloudy coupled planetary boundary layer (PBL) during a module upwind of SCI from RF21. Panel b: a typical module flown in the decoupled PBL during a downwind module from RF08.

topped, decoupled PBL (panel b). In both cases, level legs were flown near the surface (about 30 m above sea level) and about 50 m above cloud top. In addition, both modules shown feature a spiral profile (used to estimate cloud base and top/inversion heights) and a cloud top sawtooth leg to characterize vertical microphysical gradients and the entrainment interfacial layer. When clouds were greater than about 150 m thick, level legs were flown just above cloud base, about halfway between cloud base and cloud top (labeled "mid-cloud" in Fig. 4), and just below cloud top. Cloud layers were often thinner in decoupled PBLs and in the presence of strong wake mixing. In such cases, the mid-cloud and cloud top level legs were omitted. Wake mixing also occasionally caused variability in cloud base height such that no single level was representative of cloud base over the duration of a 10 minute leg; in such cases, the "cloud base" leg was also flown as a sawtooth. Finally, in decoupled conditions the mid-cloud and cloud top level legs were replaced by two level legs in the sub-cloud layer intended to quantify fluxes from the surface mixed layer into the conditionally unstable layer above ("flux legs" in Fig. 4b). The levels for the flux legs were visually identified during spiral profiles as large vertical gradients in dewpoint temperature.

3 Instrumentation

The scientific payload for SCILLA is listed in Tables 2 (facility instrumentation) and 3 (guest instrumentation). Table A1 shows the status of all instruments for each research flight. An in-depth discussion of the standard facility instrumentation suite is given in Sorooshian et al. (2018) with several notable additions: a LiCOR LI-7500a fast carbon dioxide and water vapor analyzer; a TSI 3789 water-based condensation particle counter (CPC); an Artium FPDR-PDI dual-range phase Doppler interferometer (PDI) for cloud drop size distribution measurements; nadir- and zenith-pointing Kipp & Zonen modified CM22 pyranometers for solar irradiance; and nadir- and zenith-pointing Kipp & Zonen modified CG4 pyrgeometers for infrared

https://doi.org/10.5194/essd-2026-593
Preprint. Discussion started: 4 September 2026

Open Access Earth System Science Data Discussions

irradiance. A modified Cloud Droplet Probe (CDP; Droplet Measurement Technologies, Inc., Boulder, CO) was flown but data are not included here due to technical issues with data collection and post-processing. All facility instrumentation operates at sampling frequency $f_s \geq 1$ Hz.

4 Post-processed observations

A full description of variables contained in publicly released data files is given below, sorted by category. For each variable, a list of instruments from which the measurement was derived is given as well as the reported sample frequency (or frequencies).

4.1 Merged files

The majority of measurements taken during SCILLA are reported at 1 Hz frequency and are bundled together to produce one file per flight to simplify analysis. The merged 1 Hz data files are in netCDF format and are publicly available for download and a subset of measurements recorded at $f_s \geq 10$ Hz are also bundled in merged 10 Hz netCDF files (Witte et al., 2025a, 2026a). Select measurements were taken at sampling frequencies higher than 10 Hz; we denote those datastreams available at $f_s >$ 10 Hz in the descriptions below and can provide higher frequency data upon request. Finally, data collected at $f_s < 1$ Hz (e.g., non-refractory aerosol composition) are available on an instrument-by-instrument basis (Bahreini et al., 2025; Collins et al., 2025a, b, c; Metcalf et al., 2025) and from a combined sub-1 Hz data repository (Witte et al., 2026b).

4.2 Geolocation and aircraft state

All datasets report time in Universal Time Coordinates (UTC) and all measurements are synchronized via a GPS time server (Meinberg M200/GPS) aboard the aircraft. The C-MIGITS-III GPS inertial navigation system (INS) recorded the aircraft location (latitude/longitude) and pressure altitude as well as aircraft ground speed, pitch, roll, yaw, and heading. A secondary NovAtel ProPak 6 GNSS receiver served as a backup and was used as the primary source of aircraft position information during RF16 when the primary unit failed. The NovAtel unit is also the source of GPS-based altitude, the preferred altitude variable in this dataset for scientific analysis. One other altitude variable is reported from the aircraft radar system, although this measurement is only available when the aircraft is below 1 km above ground level. True airspeed is derived from the aircraft vector velocity (measured as eastward, northward, and upward components) recorded by the INS. All primary C-MIGITS-III INS and secondary NovAtel GPS measurements are recorded at a native sampling frequency of 100 Hz and reported at 1 and 10 Hz.

4.3 Meteorology (thermodynamics and winds)

The state variables temperature, dewpoint temperature, and pressure are generated from three facility instruments housed in the nose of the aircraft: thermometer, chilled mirror hygrometer (CMH), and pressure transducers. The pressure transducers are also used to derive three-dimensional winds, which are reported as horizontal windspeed, horizontal wind direction (0° is north), and vertical velocity. From the basic thermodynamic measurements, a range of further variables are derived and

https://doi.org/10.5194/essd-2026-593
Preprint. Discussion started: 4 September 2026

Table 2. CIRPAS facility instrumentation flown during SCILLA

Instrument	Acronym	Measurement	Make/model	Notes
Inertial navigation system	INS	Geolocation, altitude, ground speed and track, pitch, roll, heading	Systron Donner C-MIGITS-III	
Backup global position system	GPS	Geolocation, altitude	NovAtel ProPak 6	
Thermometer		Total temperature	Rosemount Model 102	
Chilled mirror hygrometer	CMH	Dew point temperature	EdgeTech Vigilant	
Pressure transducers		Atmospheric pressure, winds	Setra Models 239, 270	Barometric, dynamic, radome-angle transducers
Fast CO2/H2O analyzer	LICOR	Carbon dioxide and water vapor concentrations	LiCOR LI-7500A	
Passive cavity aerosol spectrometer	PCASP	Dry particle size distribution ($0.1 < D_p < 2.6$ μm)	PMS, Inc. modified by Droplet Measurement Technologies, Inc. (DMT, Inc.; now ENVEA)	Total number concentration abbreviated N_{acc}
Ultrafine condensation particle counter	UFCPC	Particle concentration ($D_p > 0.003$ μm)	TSI 3025	Total number concentration abbreviated N_{UF}
Condensation particle counter	CPCw	Particle concentration ($D_p > 0.007$ μm)	TSI 3789	Water-based; total number concentration abbreviated N_{CN}
Counterflow virtual impactor	CVI	N/A	Brechtel CVI Inlet 1204	Evaporates cloud droplets; residual aerosol sampled
Particulate volume monitor	PVM	Bulk cloud liquid water content (LWC)	Gerber Scientific PVM-100A	
Cloud-aerosol spectrometer	CAS	Aerosol/cloud drop size distribution (DSD; $0.5 < D_p < 60$ μm)	DMT, Inc. (now ENVEA) CAS	
Phase Doppler interferometer	PDI	Liquid DSD ($2 < D_p < 2000$ μm)	Artium FPDR-PDI	Total number concentration abbreviated N_d
Cloud imaging probe	CIP	Drizzle DSD ($25 < D_p < 1550$ μm)	DMT, Inc. (now ENVEA) CIP	
Pyrometer	SST	Sea-surface temperature	Heiman Heitronics KT-19.85	
Pyranometer	CM22	Solar irradiance	Kipp & Zonen modified CM22	Upwelling & downwelling
Pyrgeometer	CG4	Infrared irradiance	Kipp & Zonen modified CG4	Upwelling & downwelling
Pyranometer	SPN1	Total and diffuse solar irradiance		Downwelling only

https://doi.org/10.5194/essd-2026-593
Preprint. Discussion started: 4 September 2026

Instrument	Acronym	Measurement	Make/model	PI
CO_2 monitor	CO2	CO_2 concentration	LI-COR, Inc. LI-820 CO2 Gas Analyzer	A. Metcalf
Mini aerosol mass spectrometer	mAMS	Non-refractory particle composition	Aerodyne Research	R. Bahreini
NOx monitor	NOx	Combined NO and NO_2 concentration	Teledyne T200U	D. Collins
Oxidation flow reactor	OFR	Generates secondary aerosol from precursor gases	PI-fabricated	D. Collins
O_3 monitor	O3	O_3 concentration	Teledyne T400	D. Collins
Scanning electrical mobility spectrometer	SEMS	Dry particle distribution ($0.02 < D_p < 0.5$ μm)	Brechtel, Inc. Model 2100	A. Metcalf
Single particle soot photometer	SP2	Size distribution and coating thickness of refractory particles	DMT, Inc. (now ENVEA) SP2-D	A. Metcalf
Tricolor absorption photometer	TAP	Aerosol light absorption at 3 visible wavelengths	Brechtel, Inc. Model 2901	A. Metcalf
Water vapor isotope analyzer	WVIA	Isotopic composition of water vapor	Los Gatos Research Triple Water Vapor Isotope Analyzer-Extended Range	L. Welp

Table 3. PI-provided instrumentation flown during SCILLA

reported: potential temperature θ, equivalent potential temperature θ_e, virtual temperature T_v, virtual potential temperature θ_v, water vapor mixing ratio r_v, relative humidity (RH) and specific humidity q_v. Surface temperature is measured by a downward-looking KT19 pyrometer. All of these variables are reported at both 1 and 10 Hz.

In addition to the CMH, two other instruments measured water vapor: a LI-COR fast H_2O analyzer (measures at 20 Hz; data reported at 1 and 10 Hz), which captures high-frequency variability with fidelity but must be absolutely calibrated to a reference measurement (in this case, CMH); and a triple water vapor isotope analyzer (WVIA), which is highly accurate in absolute terms but has a slower sampling frequency than either the LI-COR or the chilled mirror (WVIA measurements are only reported at 1 Hz). The CMH was inoperable for parts of RF05 as the mirror required cleaning. Finally, spikes in CMH vapor mixing ratio to very large values (corresponding to relative humidity in excess of 150%) during vertical profiling and sawtooth maneuvers were removed using a median filter.

https://doi.org/10.5194/essd-2026-593
Preprint. Discussion started: 4 September 2026

Open Access Earth System Science Data Discussions

4.4 Turbulence

Turbulent fluxes (of momentum $\overline{u'^2}$, $\overline{v'^2}$, $\overline{w'^2}$; sensible heat $\overline{w'\theta'}$; latent heat $\overline{w'q_v'}$; and buoyancy $\overline{w'\theta_v'}$) were computed from 10 Hz measurements during level legs using the wavelet transform method as implemented in the FluxToolbox GitHub repository (Wolfe, 2025). No fluxes are available during profile or sawtooth maneuvers due to the impact of aircraft motion on measured air velocity. Velocity data were first rotated to natural coordinates and then detrended using a 200-point moving window (an approximately 2.75 km window assuming true air speed of 55 m s^{-1}). Data were also despiked during legs with known spikes in velocity measurements (RF04 module 1 mid-cloud leg; RF14 module 2 free troposphere leg; RF19 module 2 surface leg). The Morlet wavelet was used as the mother wavelet and we include contributions to fluxes from the cone of influence. Leg-average turbulent fluxes computed using the wavelet transform were within 30% of those obtained from the eddy-covariance method. Finally, turbulent kinetic energy (TKE) was computed as TKE $= \overline{u'^2} + \overline{v'^2} + \overline{w'^2}$.

4.5 Radiation

In addition to the downward-looking pyrometer described above, three other sets of radiometers were deployed: upward- and downward-looking Kipp & Zonen modified CM22 pyranometers; upward- and downward-looking Kipp & Zonen modified CG4 pyrgeometers; and an upward-looking SPN1 pyranometer. The CM22s and SPN1 measure broadband shortwave (solar) irradiance from 0.2-3.6 µm. The SPN1 measures both the total and diffuse solar irradiance. The CG4s measure broadband longwave (infrared) irradiance from 4.2-42 µm.

4.6 Inlets

Three inlets were used for aerosol and trace gas sampling, the first two of which are described in greater detail in Sorooshian et al. (2018). The forward-facing sub-isokinetic inlet, informally known as the “snorkel,” samples aerosol less than 3.5 µm in cloud-free conditions. In cloudy conditions, a Brechtel, Inc. Model 1204 Counterflow Virtual Impactor (CVI) inlet isolates and evaporates cloud droplets and the resulting residual particles can be analyzed. The CVI has a cutoff diameter of approximately 11 µm using an add-flow rate of 16 L min^{-1} below which drops are not sampled. For RF04 only, the add-flow rate was set to 23 L min^{-1} and the cut diameter was 13.2 µm. A manual three-way valve to toggle between the snorkel and CVI inlets was switched when the aircraft entered or exited cloud and the time logged by the flight scientist. Unfortunately, the switch was operated in reverse for RFs 5, 6 and 8; data from inlet-sampling aerosol instruments are effectively unusable during these flights. A CVI flag is included in the 1 and 10 Hz merged datasets to indicate which inlet is being sampled. Finally, a rear-facing inlet was used for trace gas measurements, secondary aerosol precursor gases, and stable isotopes in water vapor. The inlet consisted of a 1/2 inch 316 stainless steel guide extending through the top of the aircraft with a 90 degree bend toward the rear. PFA Teflon tubing with 1/4 inch outer diameter (OD) was fed through the guide and aligned with the end of the guide. Early in the campaign, through RF08, there was a gap between the guide and the smaller PFA tubing that allowed cabin air to be pulled through the guide and mixed into the ambient air sampled by the PFA inlet, affecting several measurements. The gap was sealed prior to RF09 which resulted in more accurate chemical and isotopic measurements.

https://doi.org/10.5194/essd-2026-593
Preprint. Discussion started: 4 September 2026

4.7 Aerosol characterization

A variety of aerosol properties were measured during SCILLA, including: bulk number concentration, clear air and in-cloud residual size distributions, secondary aerosol formation potential and non-refractory particle composition, and aerosol number, mass and absorption properties.

4.7.1 Microphysics: bulk concentration and size distributions

Unless otherwise noted, all aerosol measurements sampled from the snorkel inlet in cloud-free conditions and the CVI in cloudy conditions. Facility measurements of aerosol concentration and clear air particle size distributions are described in detail in Sorooshian et al. (2018). For bulk aerosol number concentration, two CPCs were employed: a TSI 3025 ultrafine condensation particle counter (UFCPC; size range sampled: $D_p > 3$ nm) and a TSI 3789 water-based CPC (referred to as CPCw; size range: $D_p > 7$ nm). The Passive Cavity Aerosol Spectrometer Probe (PCASP) is a wing-mounted probe that measures aerosol size distribution in the size range $0.1 < D_p < 2.6$ µm; as it is wing-mounted, it only sampled aerosol in clear air conditions. A PI-provided Brechtel, Inc. Model 2100 Scanning Electrical Mobility Spectrometer (SEMS) sampled the snorkel/CVI inlets to measure size distributions of particles between 0.02-0.5 µm diameter with a scan time of 45 s. Finally, a DMT, Inc. CCN counter was included in the payload but no data are reported because of unacceptably high noise levels. The CPCs and PCASP are included in the 1 Hz merged files (Witte et al., 2025a, 2026a) and SEMS, with its 45 s scan time, is reported separately (Metcalf et al., 2025; Witte et al., 2026b).

4.7.2 Microphysics and radiative properties: black carbon

Black carbon (BC) was measured using an 8-channel Single Particle Soot Photometer (SP2-D; DMT, Inc., now ENVEA), which detects individual BC-containing particles by laser-induced incandescence as they pass through a high-intensity 1064 nm Nd:YAG laser. The incandescence signal is proportional to refractory BC (rBC) core mass and is largely independent of particle mixing state, allowing single-particle rBC mass and mass-equivalent diameter to be quantified after calibration with fullerene soot size-selected by SEMS. Pre- and post-campaign calibration curves were averaged to determine rBC mass, and diameters were calculated assuming an rBC density of 1.8 g cm^{-3}. BC number and mass size distributions were fitted with lognormal functions to estimate concentrations outside the SP2 detection range. The SP2 scattering detectors were also used to characterize the mixing state of rBC-containing particles. The scattering detectors were calibrated using polystyrene latex spheres (refractive index = $1.59 - 0.0i$) and Mie theory was applied to relate particle diameter and refractive index to the measured scattering cross section. For rBC-containing particles, a core-shell structure was assumed, with an absorbing rBC core surrounded by a non-absorbing coating, to estimate the particle mixing state. In this study, the standard leading-edge-only method using the split detector did not perform reliably. Therefore the coating thickness was estimated from the maximum elastic scattering signal measured by the non-split detector. Since coatings can evaporate before the full scattering signal is detected, the derived coating thickness represents a lower bound on the actual coating thickness. We applied the maximum intensity scattering signal to estimate these lower bounds on BC particle coating thickness following approaches adopted in

https://doi.org/10.5194/essd-2026-593
Preprint. Discussion started: 4 September 2026

previous studies when split detector performance was compromised (Gao et al., 2007; Subramanian et al., 2010; Schroder et al., 2015). Finally, we also applied a lag-time method to further constrain the coating thickness.

In addition to the SP2, aerosol light absorption coefficients were measured with a filter-based 3-wavelength tricolor absorption photometer (TAP 2901 UV, Brechtel Inc., Hayward, CA) at wavelengths 375, 520, and 640 nm. TAP is similar to the Particle Soot Absorption Photometer (PSAP), but it can provide longer measurements using eight sampling spots on a single filter (Laing et al., 2020). TAP computes mass loading rate of light absorbing particulate matter at a specific wavelength by quantifying light absorption over time with airflow rates, wavelength dependent absorption coefficients, and assumed particle densities. The light absorption measured at 640 nm was assumed to be black carbon (Marto et al., 2021).

SP2 and TAP data are in the 1 Hz merged files (Witte et al., 2025a, 2026a).

4.7.3 Composition: mini Aerosol Mass Spectrometer (mAMS)

The non-refractory composition (organics, ammonium, sulfate, nitrate, and chloride) of ambient PM_1 aerosols, secondary aerosols formed through the oxidation flow reactor (OFR), and cloud residuals were measured by a compact time-of-flight, miniaturized aerosol mass spectrometer (mAMS, Aerodyne Research, Inc.; Jayne et al., 2000; Vu et al., 2016; Dingle et al., 2016; Bahreini et al., 2025). The instrument alternated sampling through the forward-facing snorkel line in clear-sky, OFR (in clear-sky), and the CVI when in clouds. Furthermore, due to sampling at different altitudes and ambient pressures, the instrument always sampled air through a pressure-controlled-inlet (set at ~470 mb), leading to the ideal lens pressure value of ~1.65 mb to allow for constant transmission of aerosols in the size range of ~70-700 nm vacuum aerodynamic diameter (Bahreini et al., 2008; Vu et al., 2016; Dingle et al., 2016).

The instrument was operated in the mass spectrum mode at 11 s intervals. The 11 s detection limits, defined as three times the standard deviation of average values when sampling filtered ambient air were 0.54 µg m^{-3}, 0.14 µg m^{-3}, 0.15 µg m^{-3}, 0.045 µg m^{-3}, 0.84 µg m^{-3} for organics, nitrate, sulfate, chloride, and ammonium, respectively. The organics and ammonium detection limits are higher than typical mAMS detection limits due to the fact that the instrument was not under vacuum for a few weeks before the start of the campaign, leading to higher background levels during the study period. Overall, the instrument successfully sampled on 13 out of 20 research flights. Although during several flights (in addition to these 13), the mAMS was operational, the CVI valve system was not set properly, impacting both in-cloud and clear-sky data collection, and so mAMS data are not reported on these days.

The mass spectra were interpreted following the previously established guidelines (Allan et al., 2004; Jimenez et al., 2003), and mass concentrations of the different species were calculated using the ionization efficiency of nitrate (IE_{NO3}) and relative ionization efficiency of the other species (RIE_s). The flow rate and mass calibrations with ammonium nitrate and ammonium sulfate were carried out twice during the study, and the average IE_{NO3}, RIE_{NH4}, and RIE_{SO4} and a constant collection efficiency of 0.3 were applied to all the data. Unit-mass-resolution mass spectra data were analyzed using Squirrel ToF-AMS Analysis Toolkit (v. 1.65) while high-resolution analysis was carried out in the PIKA module for ToF-AMS HR Analysis (v. 1.25). The data have been fully quality controlled and flagged based on the instrument's sampling mode (Ambient data= 0; CVI data=1; OFR data=2; Transition=3; Internal Calibration=4). In addition, data from the times when the instrument sampled through the

https://doi.org/10.5194/essd-2026-593
Preprint. Discussion started: 4 September 2026

snorkel inlet but the aircraft was likely in/at the edge of clouds were identified based on a LWC threshold of >0.01 g m^{-3} and removed from the dataset. Composition data from mAMS are reported in Bahreini et al. (2025) and in the combined sub-1 Hz repository (Witte et al., 2026b).

4.7.4 Secondary aerosol: Oxidation Flow Reactor

An oxidation flow reactor (OFR) was used to measure secondary aerosol formation potential from precursor gases sampled from the rear-facing inlet. The OFR is based on that described by Xu et al. (2024), with modifications to make the system more compact and rugged for use on aircraft. Similar reactors have been used extensively, including in the Los Angeles region (Ortega et al., 2016) and on board research aircraft (Nault et al., 2018). The OFR was operated with a constant OH exposure, equivalent to ~ 2 days of atmospheric processing for an average atmospheric OH concentration of 1.5×10^6 cm^{-3}. Sampled ambient particles were removed upstream of the OFR by a PTFE Teflon filter and then ammonium sulfate seed particles were continuously injected to maintain an approximately constant surface area concentration and encourage condensation of oxidation products. A dedicated Scanning Mobility Particle Sizer (SMPS; fabricated) always sampled the resulting particle size distributions from the OFR, while an automated 3-way valve upstream of the mini-aerosol mass spectrometer (mAMS) alternated between OFR and the standard/CVI inlets as described above in Section 4.7.3. The SMPS size distribution data are reported in Collins et al. (2025c) and composition data in Bahreini et al. (2025, use sampling mode 2 to isolate OFR-generated particles); both datasets are also available from a combined repository (Witte et al., 2026b).

4.8 Cloud microphysics

Given the focus of SCILLA on characterizing cloud properties, there were multiple measurements of cloud microphysical parameters. The Gerber PVM-100A measures bulk liquid water content (LWC) and total surface area of drops up to 50 µm (nominally), although the response function for drops of diameter $D_p > 30$ µm has been shown to drop off at smaller sizes (Wendisch et al., 2002). Despite uncertainties in the size response of the probe and known issues with the particle surface area (PSA) channel of the PVM-100A (Witte et al., 2018), we still report those measurements as well as PVM-100A effective radius r_e. The probe is analog and therefore can be sampled at an arbitrary frequency. The Twin Otter data acquisition system samples the PVM-100A at 100 Hz and data are reported at 1 and 10 Hz.

All the other microphysical measurements for SCILLA were derived from single particle size-resolving probes flown on the aircraft wing. The Cloud, Aerosol and Precipitation Spectrometer (CAPS; DMT, Inc., now ENVEA) is a multi-probe system that consists of an aerosol spectrometer (PCASP; described above in Section 4.7.1); a hot wire bulk LWC probe (inoperable during SCILLA); a Cloud-Aerosol Spectrometer (CAS); and a Cloud Imaging Probe (CIP).

CAS measures the size and and concentration of particles 0.6-50 µm in diameter in 20 irregularly spaced diameter bins using the forward scattering technique. As particle sizing is based solely on the intensity of scattered light, large accumulation and coarse mode aerosol particles are detected in addition to liquid water droplets. We therefore recommend omitting $D_p < 2$ µm when calculating bulk moments of the cloud drop size distribution from CAS. Bulk moments reported (LWC, cloud drop number concentration N_d, r_e) follow this convention. CAS data are collected and reported at 1 Hz frequency.

https://doi.org/10.5194/essd-2026-593
Preprint. Discussion started: 4 September 2026

CIP measures particles 25-1000 µm in diameter using 64 photodiodes of constant 25 µm width. Particles are detected and sized asynchronously as they pass between a light source and the diode array, thus shading the diodes. We recommend only using size bins corresponding to $D_p > 100$ µm (i.e., more than 4 diodes shaded) due to known issues with quantification of sample volume for small drops relative to the probe size resolution (Strapp et al., 2001). CIP records drop arrivals asynchronously and can be processed to arbitrary sampling frequency. However, in light of the small drizzle drop concentrations typically observed during SCILLA we only report CIP data at 1 Hz.

The dual-range Phase Doppler Interferometer (PDI; Artium Technologies, Inc.) sizes individual cloud droplets using light scattering interferometry, with laser wavelength as the fundamental measurement scale rather than signal intensity, and is a standard method used in spray science. The technique is inherently selective for spherical or quasi-spherical droplets, reducing false detections relative to other single-particle light scattering methods, while off-axis detection provides a well-defined sample volume (Chuang et al., 2008). The PDI instrument used during SCILLA nominally measures drops from 2 µm to ~1000 µm, a range defined by the instrument settings used and the dynamic range of the instrument photodetectors. In practice, very few drops larger than 800 µm were observed. Also, the concentration of drops smaller than 4 um can not be confidently reported due to uncertainties in the instrument view volume, so values in the 2 to 4 µm size range should be treated with caution. The large size range (factor of 500 in diameter) is achievable because the instrument deployed uses two separate PDI instruments in a single package. Each separate PDI instrument, or “channel,” has its own electronics, transmitting optics, receiving optics, photodetectors, and signal processor and therefore each channel can be considered as an essentially independent instrument. Channel 1 is designed to measure smaller drops, with a size range of 2 to 65 µm, while Channel 2 measures drops between 30 and 1000 µm. The dynamic range of each channel is approximately 30:1 in terms of diameter. The primary difference between the two channels is that Ch. 2 has a much larger laser beam diameter and a larger effective slit width in the receiver, which is permitted because the concentration of drops in its measurement range is much lower than for Ch. 1. This allows for a larger view volume without significant coincidence, which occurs when two or more drops pass through the view volume at the same time, and can lead to mis-counting and/or mis-sizing of drops. The overlap between these channels allows for checking on any measurement and data analysis issues. If both channels are working properly, we expect good agreement in the overlap range, which was the case during SCILLA.

One unexpected issue that we encountered in the SCILLA data were a number of very short duration periods in which measurements were expected but no drops were recorded. We refer to these periods as data “drop-outs.” Typical durations are in the range of 0.02 to 0.1 s, with some periods exceeding several seconds, and we attribute these to unexpected buffering overflows in the signal processors. The result of this issue is that the number of drops measured in any given time interval is fewer than expected. To account for this, we use 100 Hz data from the Gerber PVM-100A, which has a much larger view volume as it measures population scattering rather than single drops. When the PVM is measuring significant cloud liquid water, but the PDI does not, then we assume the PDI experienced a data drop-out. This allows us to correct the “on” time of the PDI to produce an accurate estimate of the amount of air sampled in any given time interval. Additionally, predictable periods of time exist where the PDI is intentionally left off. Each data acquisition is collected over a duration of 30 s. This is to maintain smaller file sizes and mitigate loss of data in the unlikely occurrence that the system fails in-flight. Between each

https://doi.org/10.5194/essd-2026-593
Preprint. Discussion started: 4 September 2026

data acquisition period, there is ~2 s during which data is not collected. These periods must also be accounted for to produce an accurate estimate of sampled air. The SCILLA data product contains a variable that gives the fraction of time in every 1 Hz (or 10 Hz) time interval that the PDI was operational, including data drop-outs and periods between acquisition, so users can determine the reliability of the data. This is the first time we have observed data drop-outs, and it may be associated with the instrument being more than 15 years old (it was the first dual-range flight instrument ever built). Updates to the software and signal processors by the manufacturer are expected to eliminate this issue in the future.

The final data product is a single drop size distribution from 2 to 1000 µm which merges the two channels in the overlap range to produce the best estimate of the cloud drop size distribution for the full range. In other words, we do not report Ch. 1 and 2 as separate data products. This merged product is determined by weighting the concentration in the overlap range proportionally to the sample volume for each drop size bin. At the lower end of the overlap region, the view volume ratio between Ch. 1 and Ch. 2 is approximately 60:40, thus Ch. 1 is weighted more heavily in this region. At ≈38 µm, the weighting ratio becomes equally split, then gradually shifts to approximately 20:80 at the upper end of the overlap region where Ch. 2 has a much larger sample volume relative to Ch. 1. An example of Ch. 1, Ch. 2, and merged distributions averaged over RF04 is shown in Fig. 5.

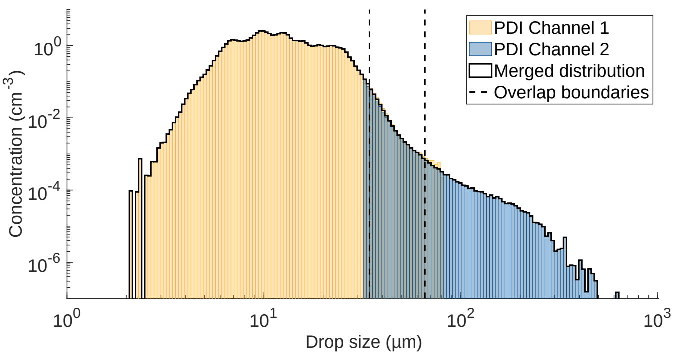

Figure 5. Merged PDI drop size distribution as a function of drop diameter averaged over all data collected during RF04.

Finally, as mentioned in Section 3, a Cloud Droplet Probe was also deployed to measure the cloud DSD. Despite passing calibration tests, data collected by the probe were found to be unusable and are not reported.

4.9 Trace gases

Several trace gas species were measured for two purposes: 1) elevated carbon dioxide (CO_2), nitrogen oxides (NO_x) and ozone (O_3) are indicators of air pollution that provide information independent of the aerosol measurements and 2) trace gases can be used to quantify entrainment mixing across the boundary layer-topping inversion.

https://doi.org/10.5194/essd-2026-593
Preprint. Discussion started: 4 September 2026

4.9.1 Water vapor isotopes

A Los Gatos Research, Inc. (LGR) Triple Water Vapor Isotope Analyzer (WVIA; model 911-0034) measured water vapor mixing ratio (q_v), δD, and δ^{18}O at 1 Hz. The WVIA was configured in extended-range mode recommended for low q_v observations with an internal cell pressure of 80 Torr. The WVIA sampled from the rear-facing inlet which included 48 cm of unheated tubing protruding through the top of the aircraft connected to a 4 m heated sampling line inside the cabin flowing at 5-10 L min^{-1}. The flow rate in the main inlet varied on different flight days during inlet troubleshooting. The WVIA sampled from the main inlet through a 6.5 cm low-flow pickoff at the analyzer's internal pump speed of 200 cm^3 min^{-1}. Cavity pressure and temperature were observed to vary (1σ) by ±0.01 Torr and ±0.17°C, respectively, over a vertical profile descent on average. The LGR observations were post-processed to screen for periods of poor data quality, to correct for time lags between the analyzer measurements and in situ sensors, and to calibrate water mixing ratios and stable isotope values. The LGR reports humidity as specific humidity in parts per million volume (ppmv).

For research flights 1 through 8, a leak in the rear-facing inlet led to the sampling of a mixture of cabin air and outside air, resulting in inaccurate q_v and isotopic values. On some other days, high q_v spikes were observed, likely caused by liquid water drops entering the rear-facing inlet. These artifacts were manually removed before performing the water calibration by comparing LGR measurements with the cabin humidity data and removing these extreme outliers.

Air sample travel through the tubing and manual LGR clock synchronization errors resulted in time lags between LGR measurement and in situ measurements which varied slightly each day due to manual clock synchronization and day-to-day differences in the main inlet flow rates. This lag was corrected by comparing LGR with in situ humidity measurements from the chilled mirror hygrometer sampling in the aircraft nose. To approximate the LGR analyzer smoothing due the residence time of air in the optical cavity, a rolling 25-second mean was applied to the in situ data. For each flight, the LGR time adjustment (typically 4–9 seconds) was identified by maximizing the correlation between the LGR 1 Hz and the in situ rolling mean humidity measurements using 1-second shifts. The 25 second rolling mean window size and day-to-day delays that performed the best were selected on the basis of the highest correlation coefficients.

LGR specific humidity measurements were also calibrated using the chilled mirror hygrometer as a reference. First, the chilled mirror hygrometer was screened for spikes in humidity during sawtooth flight patterns at cloud top due to rapid changes in temperature and humidity which caused brief periods of liquid water formation on the mirror during descending flight segments when the mirror was still colder than the cloud top air that was being sampled. Spike removal was performed by computing a rolling median within each sawtooth segment to define the local baseline. Data points exceeding this baseline by more than 0.5 g kg^{-1} were excluded. The LGR humidity measurements were then calibrated separately for each flight using a linear regression with the in situ humidity data. The slopes were mostly stable between flights (0.94 to 1.04) but the intercepts exhibited greater variability ranging from -1 to 3985 ppm.

LGR stable isotopic measurements were calibrated for known non-linear dependence on humidity (Sturm and Knohl, 2010; Salmon et al., 2019) which we corrected for using calibration experiments on the ground before, between, and after flights. A LGR Water Vapor Isotope Standard Source (WVISS; model 908-0004-9003) generated vapor with isotopic compositions

https://doi.org/10.5194/essd-2026-593
Preprint. Discussion started: 4 September 2026

between -14.4 and -84.6 ‰ in δ^18O and -87.3 and -488.6 ‰ in δD and spanning 510 ppm to 23487 ppm in q_v. We found differences in the humidity-dependent isotopic relationships between isotopically enriched and depleted standards, so we created a two-dimensional calibration surface with humidity and the measured isotopic value for each δD and δ^18O, similar to approach used by Galewsky (2021). Uncertainty of the WVIA isotopic measurements is also dependent on humidity and reported as the sum of calibration error and instrument precision. The residuals of the WVISS measurements after applying the calibration routine were used to quantify the uncertainty of the isotopic calibration. Instrument precision was quantified by the mean 1σ standard deviation for 20 seconds of measurements from the calibration experiments which increases with decreasing humidity following a power law. Each isotopic value is reported with an uncertainty that is q_v dependent.

4.9.2 Other trace gases

We used Teledyne-APi models T200U and T400 to measure NO_X and O_3 concentrations, respectively. Though the T200U can measure NO and NO_2 through alternating use of a photolytic NO_2 converter, it was operated in total NO_X mode to minimize sampling time. A LI-COR,Inc. LI-820 CO2 Gas Analyzer was used to measure CO_2 concentration.

The CO_2 data are included in the 1 Hz merged data (Witte et al., 2025a, 2026a) while NO_X and O_3 are reported individually in Collins et al. (2025a) and Collins et al. (2025b), respectively and are also available from a combined repository (Witte et al., 2026b).

5 Auxiliary data products

5.1 Flight reports

A short report was written for each research flight to provide context on the goals of the flight, details on in-flight decision making (e.g., reasoning for a shift in altitude during a level leg), and any other relevant notes that may help data users interpret the measurements. These reports are publicly available for download (Witte et al., 2025b) and we strongly recommend data users read the reports for flights they wish to analyze.

5.2 Forward cockpit video

A forward-facing camera was operated in the cockpit of the Twin Otter during each flight. The videos are publicly available to download (Witte et al., 2025c). We note that playback was accelerated to 4x realtime for the uploaded videos to reduce the amount of data storage required.

6 Overview of Flights

The purpose of this section is to give potential users of SCILLA data a reference to establish which flights they may wish to analyze based on their specific research interests. Research flights are grouped together by horizontal sampling strategy. The

https://doi.org/10.5194/essd-2026-593
Preprint. Discussion started: 4 September 2026

following shorthand will be used: N_{UF} for aerosol number concentration from the ultrafine CPC, N_{CN} for condensation nuclei (CN) number concentration from the water-based CPC, N_{acc} for accumulation mode aerosol number concentration measured by PCASP, N_d for cloud drop number concentration measured by PDI, and N_{BC} for black carbon number concentration measured by SP2. Uncertainty is quantified by standard deviation unless otherwise noted.

6.1 Aerosol characterization: Los Angeles outflow

Two aerosol characterization flights (RFs 09 and 11) sampled over the Los Angeles basin and outflow from the basin just offshore of the Malibu area.

6.1.1 Research Flight 9, 16 June 2023

RF09 sampled the spatial distribution of aerosol and trace gases in the vicinity of the Los Angeles coast using a combination of deep soundings via missed approaches at Torrance and Santa Monica airports, along with "racetracks" just offshore of Malibu and Oxnard. The racetracks are stacked level legs at 900, 1200, and 1500 m. While low clouds were present in much of the region during the flight, these were not sampled. The atmospheric thermodynamic structure is fairly consistent among all of these locations. A sharp temperature inversion of ≈5 K occurs just below 1000 m, along with a weak moisture jump of ≈ -2 g kg^{-1}. The boundary layer aerosol was also quite consistent among all locations, with $N_{acc} \approx 500$ cm^{-3} and $N_{CN} \approx 5000$ cm^{-3}. The Torrance missed approach exhibits significantly larger N_{BC} values relative to the other locations, which we speculate could be due to the proximity to the Port of Long Beach. The free tropospheric aerosol properties were highly variable. Sometimes it strongly resembled the boundary layer, while at other times it was much cleaner, with N_{CN} values 5 times smaller (≈1000 cm^{-3}).

6.1.2 Research Flight 11, 20 June 2023

RF11 sampled the spatial distribution of aerosol and trace gases downwind of the LA area at a number of locations on a day when clouds were fairly sparse in the area. The first is between San Diego and SCI, which we hypothesize is an area influenced by pollution from the LA basin when the Catalina Eddy is well-established. Next was sampling over the LA metropolitan area, with missed approaches of Long Beach and Santa Monica airports at the beginning and end of this sampling stretch. Last was a set of four racetracks off the coast of Oxnard at 900, 1000, 1200, and 1500 m (a repeat from RF09). The atmospheric thermodynamic structure was similar among all these locations. The top of the boundary layer is around 600 m altitude, but there is no sharp temperature inversion. Instead, free tropospheric θ gradually increases by ≈1 K per 100 m up to the maximum sampled altitude of 1500 m. The moisture profile shows a similar absence of a sharp transition, and instead a gradual drying with altitude, decreasing by ≈ -1 g kg^{-1} per 100 m. These profiles are consistent with the generally cloud-free conditions on this day.

The aerosol properties correlate strongly with the thermodynamic properties. Boundary layer aerosol concentrations of N_{acc} ≈500 cm^{-3} and N_{CN} ≈7000 cm^{-3} are consistent with values during RF09. In the free troposphere, these values gradu-

https://doi.org/10.5194/essd-2026-593
Preprint. Discussion started: 4 September 2026

ally decrease, reaching values of N_{acc} <200 cm^{-3} and N_{CN} ≈1000 cm^{-3} at 1500 m altitude. Nitrate mass concentration and N_{BC} also decrease with altitude. Overall, the atmospheric profiles on this day are consistent with mixing of cooler, moister and more polluted boundary layer air with cleaner and drier free tropospheric air, with strong vertical gradients across a layer that is ∼1000 m thick.

6.2 Aerosol characterization: Downwind of San Clemente Island

The other two aerosol characterization flights (RFs 12 and 20) sampled downwind of SCI.

6.2.1 Research Flight 12, 21 June 2023

The first of the clear air flights downwind of SCI was RF12 on 21 June 2023. This flight included 3 sampling modules flown along north-south oriented transects about 30, 42 and 60 km east (downwind) of the island. Visible satellite imagery showed broken stratus upwind of SCI and near the California coast (which was sampled during takeoff) that dissipated over the course of the flight; the area in which the sampling modules were flown was predominantly clear. Throughout the flight, a layer of enhanced aerosol concentration ($N_{CN} > 4000$ cm^{-3}, $N_{acc} > 250$ cm^{-3}) was observed from about 600-1200 m ASL. The inversion height was about 400-500 m (lower near the island, higher downwind) and a wake in the lee of SCI was evident in latitude-height cross-sections: horizontal wind speed aloft was at a minimum (<2 m s^{-1}); wind direction was highly variable (robustly northwesterly otherwise); and there was relatively low q_v along with enhanced aerosol concentrations during level legs flown just below the inversion. While non-refractory composition data are unavailable for this flight, SP2 N_{BC} above the inversion was about double the concentration in the PBL. During the module nearest the island, the wake spanned most of the leg (from 32.85N to 33.05N) while evidence of wake mixing was more localized further downwind (from 32.95N to 33.05N). This is consistent with the V-shaped clear areas frequently seen in the wake of SCI in satellite imagery. Finally, despite the thermal inversion strength being comparable for all 3 modules, the vapor gradient was more gradual for the module nearest the island, with a more typical "jump" of about -4 g kg^{-1} at the PBL top further downwind.

6.2.2 Research Flight 20, 29 June 2023 (afternoon)

The other aerosol-focused flight near SCI was RF20 on 29 June 2023, the sole afternoon flight of the campaign. This flight included 2 sampling modules flown along north-south oriented transects approximately 33 and 54 km east of the island. At the end of the flight, a sawtooth pattern through the top of the boundary layer was flown on the return to base. Visible imagery showed a thin, dissipating layer of broken stratus in the southern half of the flight area that was sampled during vertical sounding maneuvers but not by any level legs. Similar to what was observed during the morning flight (RF19), enhanced aerosol concentrations were observed by the aerosol particle counters above the boundary layer. Unlike RF19, areas of higher particle counts were more localized in the inversion (≈500 m), with a notable peak in total aerosol concentration ($N_{UF} > 8000$ cm^{-3}) between 32.8-32.9°N during the wake module and from 32.6-32.75°N during the downwind module. A more persistent layer of enhanced N_{UF} was observed near 800 m altitude during both modules. Interestingly, N_{acc} and N_{BC} were lower in the area

https://doi.org/10.5194/essd-2026-593
Preprint. Discussion started: 4 September 2026

of large fine mode concentrations during the wake module, suggesting a distinct aerosol population from the layer aloft near 800 m.

6.3 Island wake/downwind characterization

A total of four flights were flown to characterize the wake of SCI and downwind evolution of the PBL: RF03 (9 June), RF08 (15 June), RF13 (22 June) and RF17 (27 June). These flights each had a unique horizontal sampling strategy based on the airspace in which the Twin Otter was cleared to fly, i.e., flight plans were adapted to the available airspace.

6.3.1 Research Flight 03, 9 June 2023

RF03 on 9 June 2023 was flown in a "chevron" pattern south and east of the southeastern tip of SCI. This pattern was chosen due to the prevailing northwesterly flow in the boundary layer. The chevron pattern consisted of a stack of level legs (at standard heights for the coupled PBL) split between E-W and N-S headings. A third partial module sampled cloud top variability parallel to the N-S headings about 45 km to the E of SCI. The boundary layer was quite deep during this flight with an inversion height of about 1 km. The PBL was close to coupled (or very slightly decoupled, depending on one's perspective) with a thermal jump of about 8 K and a vapor jump of -3 g kg^{-1} across the inversion. The PCASP indicated N_{acc} about twice as abundant above the inversion as compared to the surface legs, where $\overline{N_{acc}} = 211 \pm 27$ cm^{-3}. Compared to later flights with lower inversions, there was no evidence of increasing N_{acc} with distance downwind of the island. The maximum observed PDI $N_d \approx 400$ cm^{-3} was consistent with the above cloud PCASP N_{acc} measurements. Despite a cloud depth approaching 400 m, very little drizzle was observed; N_d was likely high enough to suppress collisional growth of drops. Overall, there was little evidence of the island significantly disturbing the boundary layer flow during RF03, but the vertical gradient in N_{acc} is suggestive of some downward mixing of particulates through the inversion and into the PBL.

6.3.2 Research Flight 08, 15 June 2023

RF08 on 15 June 2023 consisted of two decoupled PBL sampling modules, one just downwind of SCI ("wake" module) and another about 30 km to the east ("downwind" module), followed by an along-flow cloud top sawtooth leg before the return-to-base ferry. Contrary to most of the other flights, the downwind module was flown first because satellite imagery indicated that the cloud deck was dissipating, with clearing spreading from the eastern flank of Catalina Island to the southeast. Winds were from the W to NW and were fairly weak (typical $U \sim 2$ m s^{-1}) in the PBL with higher speeds ($U \sim 6$ m s^{-1}) above. The PBL was weakly stable up to the capping inversion, the height of which was highly variable (820-1100 m) across modules and overall higher during the wake module. While the thermal jump was fairly well defined ($\Delta\theta \approx 9$ K), there was almost no moisture jump at the inversion, and in fact a small "bump" to higher q_v values was noted around 1100 m during both modules. Despite the stable PBL, the cloud layer was quite thick, spanning almost 600 m during the wake module and 400 m during the downwind module. As a result, rather large values of LWC for stratocumulus (> 1 g m^{-3}) were observed with typical N_d between 100-200 cm^{-3}. Abundant drizzle was measured during the sub-cloud and surface legs of both modules.

https://doi.org/10.5194/essd-2026-593
Preprint. Discussion started: 4 September 2026

The boundary layer was quite clean with CN concentrations of 300 cm^{-3} or less. Aloft, concentrations were much higher, with above cloud N_{CN} averaging about 3000 cm^{-3} during both modules and spatially isolated regions with concentrations exceeding 5000 cm^{-3}. The latter regions contained large accumulation mode aerosol counts ($N_{acc} \approx 1000$ cm^{-3}) as well, potentially indicating an aged airmass. There was a notable covariance between high aerosol regions aloft and enhanced θ_e, which points to a continental origin for those large aerosol concentrations. Turbulence was generally weak in the cloud layer and at the surface (surface leg mean TKE $= 0.12 \pm 0.05$ m^{2}s^{-2}) although values approaching 1 m^{2}s^{-2} were observed near cloud base.

6.3.3 Research Flight 13, 22 June 2023

RF13 consisted of three complete coupled PBL sampling modules flown along north-south headings approximately 15, 45 and 75 km downwind of SCI (termed the "wake", "downwind," and "recovery" modules, respectively). A well-defined V-shaped wake was present in satellite imagery and was reflected in latitude-altitude cross-sections of the aircraft measurements. In the cross-sections, the wake manifests as a pronounced minimum in wind speeds and relatively high θ_e and q_v during the level legs in the PBL. The inversion height was around 750 m with jumps of $\Delta\theta \approx 8$ K and $\Delta q_v \approx -7$ g kg^{-1}. Clouds were found only in the low level convergence zone during the wake module and more ubiquitously during the downwind and recovery modules. During all modules, N_d was rather variable: during the wake, downwind, and recovery modules, the mean N_d was $\{248, 281, 320\}$ cm^{-3} and the interquartile range was $\{245, 272, 367\}$ cm^{-3}, respectively. Despite these large ranges of N_d, aerosol counts were relatively low. Mean aerosol concentrations in the PBL were $\overline{N_{UF}} = 970 \pm 118$ cm^{-3} and $\overline{N_{CN}} = 712 \pm 231$ cm^{-3}. Values were generally lower above the PBL, although there was a spike to around 1500 cm^{-3} at the north end of each module between 700-850 m. In the PBL, PCASP $\overline{N_{acc}} = 250 \pm 58$ cm^{-3}, suggesting that some N_d activated on Aitken mode aerosol. Moderate to strong turbulence (in-cloud level leg mean TKE $= 0.57 \pm 0.29$ m^{2}s^{-2}) is consistent with this interpretation.

6.3.4 Research Flight 17, 27 June 2023

Two modules were flown during RF17: a long (~ 60 km) "wake" module about 15 km east of SCI, and a standard-length (30 km) "downwind" module about 45 km east of the island. Both modules were flown on N-S headings. Due to the expanded length of the wake module, the surface leg was split into two 5-min segments at the beginning and end of the module and additional 5-min level segments were flown about 200 m above cloud top to sample the local maximum in above-cloud aerosol loading. The wake morphology was complicated, with some evidence for vortex shedding but a fairly consistent V-shape as well. At the same time, the cloud deck quickly retreated from the coast. During the descending profile of the wake module, a ~ 200 m layer of high aerosol loading ($N_{CN} > 4000$ cm^{-3}, $N_{acc} > 500$ cm^{-3}) was observed. The boundary layer was substantially cleaner ($\overline{N_{CN}} = 549 \pm 334$ cm^{-3}, $\overline{N_{acc}} = 263 \pm 70$ cm^{-3}), although $\overline{N_{acc}}$ was higher during the downwind module by about 50 cm^{-3}. Despite the vertical separation between the cloud top/inversion and the polluted layer aloft, mean $N_d = 455 \pm 115$ cm^{-3} during the flight with an observed maximum of nearly 750 cm^{-3}. Both modules exhibited LWC profiles fairly close to adiabatic with peak LWC $\approx 0.5 - 0.6$ g m^{-3}.

https://doi.org/10.5194/essd-2026-593
Preprint. Discussion started: 4 September 2026

Open Access Earth System Science Data Discussions

6.4 Island wake edge characterization

Flights focused on characterizing the edge of the island wake differed from the "downwind wake characterization" flights in that the wake edge flights typically sampled a single, long transect in the island wake (RF05, RF10) or in different angles downwind of the island (RF06) while the downwind wake characterization flight modules sampled along the same downwind region at multiple distances leeward of SCI.

6.4.1 Research Flight 05, 11 June 2023

The flight pattern for RF05 included two N-S oriented modules from a common sounding point (approximately 32.91N, 118.14W) about 30 km downwind of SCI. One module was flown to the north of the sounding point and the other to the south, followed by a final descending profile before returning to base. The PBL was weakly stable above 300 m with a more pronounced inversion aloft, starting between 1600 and 1800 m depending on the module. Winds in the low levels (below about 700 m) were northerly at about 5 m s^{-1}; from 700 to about 1500 m, the direction was northeasterly and speeds decreased to about 2 m s^{-1} before increasing again aloft; above 1500 m, the south and north modules disagreed on wind speed (faster to the south) and direction (during north module, turning with height from northeasterly to northwesterly). Cloud vertical structure was complicated but generally resembled cumulus under stratocumulus. Some level leg segments were distinctly cumuliform with $w > 2$ m s^{-1} and LWC > 1 g m^{-3}, while others were obviously stratiform (i.e., far above the LCL predicted from the surface leg but with weaker w and commensurately lower LWC values). Regarding the latter, it is not straightforward to draw a clear distinction between cloud formed by detrainment versus active updrafts. In terms of aerosol loading, the sub-cloud layer was quite clean ($N_{CN} < 500$ cm^{-3}, $N_{acc} < 250$ cm^{-3}) with a layer of higher aerosol concentrations ($N_{UF} > 1500$ cm^{-3}, N_{acc} >500 cm^{-3}) spanning about 1500-1800 m. There is a corresponding vertical gradient in cloud N_d with values generally < 20 cm^{-3} below 1 km and a jump to higher, if rather variable, values near cloud top $\overline{N_d} = 186 \pm 150$ cm^{-3}) with peak N_d nearing 800 cm^{-3}.

6.4.2 Research Flight 06, 12 June 2023

RF06 consisted of two sampling modules flown downwind of SCI: the first ∼30 km northeast of the island on a NW-SE line and the 2nd ∼45 km east of the island on a N-S line. Satellite imagery showed a marked decrease in cloud brightness to the east of SCI and an obvious change in cloud texture to the west of the Point Conception hydraulic jump, with broken clouds to the west and a more uniformly overcast scene to the east. The structure of the wind profiles was quite complicated this day, with minima in wind speed around 600 and 1300 m delineating three "regions:" primarily northerly winds from 0-600 m; primarily southerly winds from 600-1300 m (although the 2 modules have opposing zonal directions from 600-800 m: easterly component during module 1, westerly during module 2); then back to the expected northwesterly flow above 1300 m. Wind speeds were low throughout the profile, about 6 m s^{-1} above the PBL ($z > 1300$ m) and < 5 m s^{-1} below. In terms of thermodynamics, the profile was stable above about 200 m with a pronounced inversion layer at 1200-1300 m. This indicates that the elevated cloud layer (base height ∼1 km) was decoupled from the surface. Below the cloud layer, the air was quite

https://doi.org/10.5194/essd-2026-593
Preprint. Discussion started: 4 September 2026

clean with $N_{UF} < 1000$ cm^{-3} and $N_{acc} < 200$ cm^{-3}. Above cloud, some isolated patches of higher aerosol loading were observed (maximum $N_{acc} \approx 600$ cm^{-3}, maximum $N_{UF} \approx 3000$ cm^{-3}). It was also very clean in cloud during module 1: $\overline{N_d} = 55 \pm 19$ cm^{-3} (maximum $N_d = 136$ cm^{-3}). There was some evidence for cross-inversion aerosol mixing during module 2, where $\overline{N_d} = 151 \pm 74$ cm^{-3} (maximum $N_d = 371$ cm^{-3}). Despite the complicated wind and thermodynamic structure, the cloud vertical structure was fairly well-behaved, with a ∼200 m thick nearly adiabatic cloud layer observed during module 1. The structure was more complex during module 2, with a comparable stratus layer from 1100-1300 m but another low LWC (< 0.2 g m^{-3}) layer above (roughly 1300-1500 m) and drizzle observed during the spiral sounding. There was also a strong latitudinal gradient during the in-cloud level legs, with greater LWC to the south and more variable N_d to the north.

6.4.3 Research Flight 10, 19 June 2023

RF10 included 3 sampling modules flown on the same NW-SE transect about 60 km downwind (east) of SCI. The first two modules were complete and the final partial module consisted of a deep sounding and cloud top sawtooth leg. Over the course of the flight, the boundary layer gradually became more stable (i.e., higher θ and lower q_v above surface mixed layer during later modules) and satellite imagery indicated a thinning cloud layer. These changes were expressed as a commensurate increase in cloud base height of ~ 200 m from module 1 to module 2. Winds were nearly slack in the boundary layer ($\overline{U} \approx 2$ m s^{-1} below 800 m) with a sudden increase to ~ 8 m s^{-1} above the inversion. The aerosol probes showed low concentrations with $N_{acc} < 300$ cm^{-3}, $N_{CN} < 800$ cm^{-3} and $N_{UF} < 1000$ cm^{-3} for all but a few seconds of the flight. This is a notable contrast with most of the other SCILLA flights, for which there was routinely at least one isolated patch of $N_{CN} \gg 1000$ cm^{-3} observed aloft. Despite the relatively clean lower atmosphere, $\overline{N_d} = 233 \pm 91$ cm^{-3} with a maximum observed value of 590 cm^{-3}, suggesting that numerous Aitken mode aerosol may have been activated. Finally, plentiful drizzle was observed during the first module, which is somewhat surprising given $\overline{N_d} > 200$ cm^{-3}.

6.5 Open ocean/upwind marine boundary layer characterization

Two research flights were flown upwind of San Clemente Island: RF07 and RF14. Both of these flights were flown west of the northwestern tip of SCI along approximately the same SW-NE oriented line. While the intent was to sample the "open ocean" environment, the area sampled during these flights was often aligned with (or in other words, downstream of) San Nicolas Island. Despite the maximum elevation of San Nicolas Island being about half that of SCI (275 m vs. 600 m, respectively), it is still possible for the boundary layer flow to be disturbed downwind of San Nicolas Island. There is limited evidence for such disturbances during RF07 and RF14, although island effects may have been more important during some of the open ocean-island wake contrast flights described in the next subsection.

6.5.1 Research Flight 07, 13 June 2023

Of all the SCILLA flights, RF07 was the most representative of "classic" non-precipitating marine stratocumulus. Two complete modules were flown along the same line during the flight. The boundary layer was well-mixed with a strong inver-

https://doi.org/10.5194/essd-2026-593
Preprint. Discussion started: 4 September 2026

sion ($\Delta\theta \approx 10$ K, $\Delta q_v \approx -5$ g kg^{-1}) beginning at $z \approx 900$ m and there was very little change in thermodynamic state between the first and second modules. Aerosol loading in the subcloud layer was low but not ultraclean, with module-mean $\overline{N_{CN}} = 539 \pm 36$ cm^{-3} and $\overline{N_{acc}} = 175 \pm 16$ cm^{-3}. Somewhat higher aerosol concentrations were observed during the above cloud leg during the first module (flown at 1050 m ASL; leg-mean $\overline{N_{CN}} = 714 \pm 280$ cm^{-3}, $\overline{N_{acc}} = 214 \pm 23$ cm^{-3}) with values quickly decreasing above. The LWC profiles were very close to adiabatic with cloud top values averaging about 0.8 g m^{-3}. In light of the low subcloud layer N_{acc}, N_d was higher than expected: during module 1, $\overline{N_d} = 316 \pm 70$ cm^{-3} and during module 2, $\overline{N_d} = 283 \pm 57$ cm^{-3}. As with many other flights, this suggests a healthy contribution to N_d from Aitken mode aerosol. Almost no drizzle was observed.

6.5.2 Research Flight 14, 23 June 2023

The flight plan for RF14 was almost identical to RF07. But while boundary layer properties were essentially static during RF07, they were rapidly evolving during RF14, during which the aircraft observed a dissipating cloud deck over the course of two sampling modules. Potential temperature θ was nearly constant in the PBL throughout the flight (flight-mean $\overline{\theta} = 288.4 \pm 2.2$ K) and the magnitude of the thermal jump at the inversion was approximately constant at $\Delta\theta = 7$ K. The inversion height was around 950 m during the first module and lowered to about 880 m during the second module and PBL q_v was higher during module 2 by about 1.4 g kg^{-1}, a considerable increase (+20%) that resulted in significant lowering of cloud base (≈ 200 m) from 800 m (module 1) to 600 m (module 2). Despite the increased humidity in the boundary layer during module 2, the cloud was rather patchy and intermittent during the "in-cloud" level legs. There was very little drizzle during either module. The subcloud layer was relatively clean (flight-mean $\overline{N_{acc}} = 201 \pm 26$ cm^{-3}, $\overline{N_{CN}} = 596 \pm 38$ cm^{-3}) with only a few isolated observations of $N_{CN} > 1000$ cm^{-3} above the cloud layer. Similar to RF07, flight-mean $\overline{N_d}$ was greater than $\overline{N_{acc}}$, although in this case about 50% higher ($\overline{N_d} = 302 \pm 111$ cm^{-3}, maximum $N_d = 688$ cm^{-3}) versus only 18% higher during RF07. This was likely due to stronger turbulence during RF14, where in-cloud TKE values > 1 m^{2}s^{-2} were frequently observed.

6.6 Open ocean-island wake contrast

6.6.1 Research Flight 02, 6 June 2023

RF02 was the first flight attempting to contrast the environment upwind vs. downwind of SCI. One complete module was flown upwind (to the southwest) of SCI and one partial module was flown to the northeast, both along E-W oriented lines. The boundary layer was anomalously deep this day, with the inversion height between 1400-1550 m (higher to the east). A decoupled state was apparent in both the θ profile, which steadily increased with height above the surface, and the q_v profile, which showed a small jump of around -1 g kg^{-1} around 300 m. Aloft, the moisture jump was coincident with the thermal inversion and the overlying free tropospheric air was extremely dry ($q_v < 2$ g kg^{-1}). Winds were near slack (mean PBL $\overline{U} = 2.4 \pm 0.9$ m s^{-1}) to the point that almost no waves were visible from the aircraft during the 30 m altitude "surface" legs. Accordingly, the boundary layer was extremely clean during the upwind module with $\overline{N_{acc}} = 39 \pm 14$ cm^{-3} and $\overline{N_{UF}} = 302 \pm 54$ cm^{-3} (the water CPC was inoperable during RF02, so no measurements of N_{CN} were available). PBL aerosol

https://doi.org/10.5194/essd-2026-593
Preprint. Discussion started: 4 September 2026

loading was substantially higher, although still far from qualifying as polluted, during the downwind module with $\overline{N_{acc}} = 107 \pm 26$ cm^{-3} and $\overline{N_{UF}} = 945 \pm 248$ cm^{-3}. Aerosol loading was also higher in the free troposphere ($\overline{N_{acc}} = 311 \pm 32$ cm^{-3}, $\overline{N_{UF}} = 1322 \pm 155$ cm^{-3}), with a local maximum just atop the PBL during both modules. The cloud field was effectively cumulus under stratocumulus and the aircraft sampled these cumulus-like features on both sounding maneuvers during the upwind module. With $\overline{N_d} = 36 \pm 34$ cm^{-3} and cloud top LWC well in excess of 1 g m^{-3} during the upwind module, rather heavy rain rates for PBL clouds ($R \gg 10$ mm hr^{-1}) were observed.

6.6.2 Research Flight 04, 10 June 2023

RF04 was the first "complete" (i.e., 2 full modules) upwind-downwind contrast flight, with a upwind module flown due west of the northwestern tip of SCI along a SW-NE line and a downwind module flown east of the southeastern tip of SCI along a N-S line. Cirrus above the boundary layer limited visibility of the low-level clouds in satellite imagery. Similar to RF02, the PBL was again quite deep with an inversion height near 1 km, although the inversion structure was spatially variable during the upwind module, in some locations reaching nearly 1.2 km. The degree of cloud-surface coupling was also ambiguous during the upwind module due to a low cloud base; a more obvious drop in q_v around 250 m was apparent during the downwind module. Substantial inter-module differences were seen in the dynamic and thermodynamic profiles as well. Below about 700 m during the downwind module, θ was about 1.5 K warmer and wind speed and q_v were lower from 200 m to the inversion ($z \approx 1$ km). Curiously, sea surface temperature (as measured by a nadir-pointing IR radiometer during near-surface level legs) was comparable across the upwind and downwind modules and therefore can't explain the warmer PBL temperatures during the downwind module. Instead, it seems more likely that low-level θ during the upwind module is set by advection over colder waters upstream. The boundary layer was clean during both modules (upwind: $\overline{N_{UF}} = 442 \pm 80$ cm^{-3}, $\overline{N_{acc}} = 182 \pm 49$ cm^{-3}; downwind: $\overline{N_{UF}} = 631 \pm 288$ cm^{-3}, $\overline{N_{acc}} = 223 \pm 31$ cm^{-3}; note that the water-based CPC was inoperable during this flight) although there was a layer of higher aerosol loading from the inversion to about 1200 m during the upwind module and 1100-1300 m during the downwind module with peak $N_{UF} \approx 1500$ cm^{-3}. There was a notable horizontal gradient in aerosol loading during the downwind module due to sampling the edge of the island wake with cleaner air to the south. Due to the relatively large differences in thermodynamic structure between modules, there were correspondingly stark differences in cloud vertical structure. Cloud base height was about 400 m during the upwind module and the LWC profile was nearly adiabatic to 900 m, above which it began to decrease (likely due to the messy inversion structure). Nevertheless, the maximum LWC measured during this module was nearly 2 g m^{-3}, an extreme value in the context of marine stratocumulus, and very high rain rates (geometric mean and standard deviation of upwind surface rain rate $\overline{R} = 8.8 \pm 4.0$ mm hr^{-1}). During the downwind module, on the other hand, cloud base was near 760 m, the LWC profile was solidly subadiabatic, and no drizzle was observed.

6.6.3 Research Flight 15, 24 June 2023

RF15 included an upwind module flown to the southwest of SCI along a SW-NE line and a downwind module flown just southeast of the island, also along a SW-NE line, roughly parallel to the upwind module. The downwind module line was twice as long as the upwind module (60 km vs. 30 km). There was thin cirrus streaming over the low-level clouds throughout

https://doi.org/10.5194/essd-2026-593
Preprint. Discussion started: 4 September 2026

the flight, which limited the availability of satellite retrievals of low-level cloud microphysical properties. Nevertheless, a distinct straight wake was apparent downwind of SCI, oriented nearly parallel with the long axis of the island (i.e., NW-SE). This flight featured some of the highest PBL wind speeds of the campaign, with $\overline{U} = 10.1 \pm 0.7$ m s^{-1} below 750 m during the initial descending profile and the direction was northwesterly. Due to these strong winds and correspondingly strong turbulence (for all upwind level legs and about half downwind, leg-average $\overline{\text{TKE}} > 0.5$ m^{2}s^{-2} and many instantaneous values > 1 m^{2}s^{-2} were observed in cloud), the cloud layer was coupled to the surface and the PBL was well-mixed. The inversion height was about 800 m and quite strong ($\Delta\theta \approx 10$ K, $\Delta q_t \approx -4$ g kg^{-1}). Condensation nuclei loading was relatively light in the PBL (upwind: $\overline{N_{CN}} = 771 \pm 225$ cm^{-3}; downwind: $\overline{N_{CN}} = 868 \pm 71$ cm^{-3}) but N_{acc} was moderate (upwind: $\overline{N_{acc}} = 241 \pm 19$ cm^{-3}; downwind: $\overline{N_{acc}} = 270 \pm 25$ cm^{-3}) and there was a layer of enhanced aerosol concentrations (about 20% higher on average for N_{acc}, 50% higher for N_{CN}) above the PBL from about 900-1100 m altitude. The strong turbulence and moderate aerosol loading resulted in $\overline{N_d} > \overline{N_{acc}}$, with upwind and downwind $\overline{N_d}$ almost identical ($\overline{N_d} = 423 \pm 147$ cm^{-3}; downwind $\overline{N_d} = 424 \pm 180$ cm^{-3}). Extreme N_d values were almost twice as high as the module means with 90th percentile for the whole flight $N_{d,90} = 770$ cm^{-3}.

6.6.4 Research Flight 16, 26 June 2023

A sustained Catalina eddy event began on 26 June 2023 that persisted through the end of the experiment on 30 June. This flight featured the usual upwind and downwind modules but, since the cloud deck was already dissipating east of the Channel Islands, they were flown in reverse order: the downwind module was flown first along an E-W line about 25 km south of the southeastern tip of SCI and the upwind module on a WSW-ENE line just off the northwestern tip of SCI. A straight wake extended ESE of the island. The inversion height was around 650 m with a strong thermal jump ($\Delta\theta \approx 10$ K) that was consistent across modules. The moisture jump was much smaller during the upwind module (-3 g kg^{-1} upwind vs. -9 g kg^{-1} downwind), evidence that two distinct free tropospheric airmasses were sampled. In addition, sampling above cloud during the upwind module showed significantly higher aerosol loading than downwind: averaged over the altitude range 650-900 m, $\overline{N_{acc}} = 708 \pm 225$ cm^{-3} and $\overline{N_{CN}} = 2645 \pm 2122$ cm^{-3} upwind while $\overline{N_{acc}} = 182 \pm 44$ cm^{-3} and $\overline{N_{CN}} = 316 \pm 305$ cm^{-3} downwind. On the other hand, within the PBL, $\overline{N_{acc}}|_{BL}$ and $\overline{N_{CN}}|_{BL}$ were comparable across modules (upwind: $\overline{N_{acc}}|_{BL} = 359 \pm 51$ cm^{-3} and $\overline{N_{CN}}|_{BL} = 776 \pm 240$; downwind $\overline{N_{acc}}|_{BL} = 384 \pm 30$ cm^{-3} and $\overline{N_{CN}}|_{BL} = 806 \pm 503$ cm^{-3}). Given the magnitude of the aerosol loading, N_d was also quite high with a flight-mean value $\overline{N_d} = 538 \pm 187$ cm^{-3} (only minor variability across modules). Despite the inter-module consistency in inversion height and N_d, there were major differences in cloud base height (upwind, ≈ 300 m; downwind ≈ 450 m) due to a much warmer PBL during the downwind module and therefore different LWC profiles. The upwind LWC profile is nearly adiabatic from cloud base (just below 400 m) to 700 m such that even with very high N_d, some drizzle was observed upwind, while the downwind profile is subadiabatic throughout (at the level of peak LWC, adiabatic fraction is about 55%).

https://doi.org/10.5194/essd-2026-593
Preprint. Discussion started: 4 September 2026

6.6.5 Research Flight 18, 28 June 2023

RF18 included a total of 4 sampling modules: 3 full "coupled cloudy PBL" modules (one upwind; one about 15 km alee of the island referred to as the "wake" module; and another $\sim$ 30 km farther east referred to as the "downwind" module) and one partial module consisting of a long, along-wake cloud top sawtooth leg to probe the recovery of the PBL. Satellite imagery showed a Catalina eddy circulation with the center of rotation just north of SCI. In addition, vortices were shed in the wake of SCI early in the flight (at least one of which was likely sampled during the wake module) before later taking on more of a straight wake morphology. The inversion height was roughly consistent across modules around 700 m (slightly higher upwind, slightly lower downwind) with $\Delta\theta \approx 10$ K. During the upwind module, there were notable longitudinal gradients in numerous variables: wind speed U was higher to the west while to the east, particle counts (N_{UF}, N_{CN}, N_{acc}, and N_d) and q_v were higher. This suggests that the aircraft sampled either the wake of San Nicolas Island and/or the edge of a continental airmass ostensibly advected by the eddy circulation. Upwind aerosol concentrations were relatively clean in the PBL ($\overline{N_{CN}}|_{BL} = 446 \pm 165$ cm^{-3}, $\overline{N_{acc}}|_{BL} = 123 \pm 36$ cm^{-3}) and while there was a slight uptick in accumulation mode aerosol loading just above the PBL (upwind 700-900 m $\overline{N_{acc}} = 220 \pm 56$ cm^{-3}), N_{CN} did not show a comparable increase. There were still very few CN in the PBL during the wake and downwind modules (wake: $\overline{N_{CN}}|_{BL} = 390 \pm 101$ cm^{-3}, downwind: $\overline{N_{CN}}|_{BL} = 289 \pm 160 \pm$ cm^{-3}), although N_{acc} increased (wake: $\overline{N_{acc}}|_{BL} = 190 \pm 18$ cm^{-3}, downwind: $\overline{N_{acc}} = 189 \pm 42$ cm^{-3}). Nevertheless, module mean N_d values were large (upwind $\overline{N_d} = 244 \pm 73$ cm^{-3}, wake $\overline{N_d} = 328 \pm 82$ cm^{-3}, downwind $\overline{N_d} = 399 \pm 102$ cm^{-3}). The largest values of N_d were observed near cloud top alee of the island, with a maximum observed value of 546 cm^{-3}. Activation of aerosol mixed down from above is consistent with very strong TKE during this flight (the strongest of the campaign) with peak values up to 2.5 m^{2}s^{-2} and level leg averages of 1-2 m^{2}s^{-2}. The flight scientist noted that it was "pretty bumpy in and around cloud."

6.6.6 Research Flight 19, 29 June 2023 (morning)

RF19 featured 3 "coupled PBL" sampling modules: one full module upwind flown about 60 km due south of San Nicolas Island on SW-NE line; one full module directly in the wake of the island (the "wake" module) on a N-S heading; and one partial module $\sim$ 30 km to the east comprised of level and sawtooth legs at cloud top (the "downwind" module), again on a N-S line. The upwind module was one of the farthest west besides RF02 and therefore one of the least likely to be influenced by flow disturbances downstream of San Nicolas Island. Mesoscale eddy activity was again apparent in satellite imagery (although the SCI wake structure was not obvious), with the center of rotation approximately equidistant from San Nicolas Island, Santa Catalina Island, and SCI. The cloud deck rapidly dissipated from the coast toward the Channel Islands over the course of the flight. Inversion height rose from about 660 m during the upwind module to 680 m during the wake module. There was a strong temperature jump ($\Delta\theta \approx 10$ K) and a very weak moisture jump ($\Delta q_v \approx -1$ g kg^{-1}). Wind speeds were faster during the upwind module by over 5 m s^{-1} regardless of altitude (upwind: $\overline{U} = 8.0 \pm 1.0$ m s^{-1}; wake: $\overline{U} = 2.2 \pm 0.6$ m s^{-1}; no sounding during downwind module). Aerosol loading in the free troposphere was significant: above 625 m, flight-mean $\overline{N_{CN}} = 2896 \pm 2973$ cm^{-3} and $\overline{N_{acc}} = 462 \pm 120$ cm^{-3}. Several "patches" of high aerosol loading were also encountered

https://doi.org/10.5194/essd-2026-593
Preprint. Discussion started: 4 September 2026

during the downwind cloud top sawtooth. In the subcloud layer, N_{acc} increased by about a factor of 2 in the lee of the island (upwind: subcloud $\overline{N_{acc}} = 131 \pm 24$ cm^{-3}, wake: $\overline{N_{acc}} = 272 \pm 25$ cm^{-3}). Consistent with many other SCILLA flights, N_d was slightly higher than N_{acc} both upwind ($\overline{N_d} = 195 \pm 58$ cm^{-3}) and in the wake ($\overline{N_d} = 289 \pm 104$ cm^{-3}). Consistent with other open ocean-island wake contrast flights, the boundary layer was about 2 K warmer during the wake module (compared to the upwind module) which resulted in cloud base being about 150 higher (cloud base height upwind: 200 m; wake: 350 m) but both upwind and wake module LWC profiles were close to adiabatic. The deeper cloud layer upwind resulted in some scattered drizzle detections during the surface leg.

6.6.7 Research Flight 21, 30 June 2023

The final flight of the campaign, RF21, included 3 "coupled PBL" modules: one complete upwind module flown west of the northwestern tip of SCI on a SW-NE line; one complete module in the SCI wake on a N-S line ("wake" module); and 30 km to the east of the wake module and also on a N-S line, a final "downwind" partial module that did not include a deep sounding or free troposphere level leg. Geostationary imagery showed continuing Catalina eddy circulation over the Bight and a cloud deck dissipating from the coast westward. The wake structure was complicated, perhaps in part due to a compressed boundary layer that resulted in some of the SCI topography poking up into the clear free troposphere. By the end of the flight, it appeared that vortices were shedding from the NW and SE tips of the island, with some hints of a straight wake oriented nearly due east of the island. As mentioned, the PBL height was very low (upwind and wake modules: 450 m; downwind: 400 m) and the inversion was very strong with $\Delta\theta \approx 12$ K. The moisture jump Δq_v was weaker, only about -3 g kg^{-1}. Wind speeds were low ($U < 5$ m s^{-1}) through the depth of the profiles during the upwind and wake modules. A pronounced spike to $U > 10$ m s^{-1} was measured over a thin layer (about 500-530 m altitude) during the final partial module, which may have been a weak low-level jet. Elevated aerosol loading was observed above cloud during both the upwind and wake modules (upwind: $\overline{N_{CN}} = 3615 \pm 153$ cm^3, $\overline{N_{acc}} = 520 \pm 73$ cm^{-3}; wake: $\overline{N_{CN}} = 2679 \pm 134$ cm^{-3}, $\overline{N_{acc}} = 666 \pm 42$ cm^{-3}; no above cloud leg during downwind module) while aerosol concentrations below cloud more than doubled from upwind to the wake: upwind $\overline{N_{CN}} = 354 \pm 93$ cm^{-3}, $\overline{N_{acc}} = 139 \pm 40$ cm^{-3}; wake $\overline{N_{CN}} = 742 \pm 167$ cm^{-3}, $\overline{N_{acc}} = 358 \pm 60$ cm^{-3}; downwind: $\overline{N_{CN}} = 848 \pm 94$ cm^{-3}, $\overline{N_{acc}} = 388$ cm^{-3}. There was a comparable increase in $\overline{N_d}$ across modules: upwind $\overline{N_d} = 188 \pm 63$ cm^{-3}; wake $\overline{N_d} = 405 \pm 199$ cm^{-3}; downwind $\overline{N_d} = 485 \pm 177$ cm^{-3}. The peak concentration observed during the flight occurred during the wake module, when $N_{d,max} = 1020$ cm^{-3}. Cloud base height z_{cb} was very low during RF21 and increased from west to east: upwind $z_{cb} = 100$ m; wake $z_{cb} = 180$ m; downwind $z_{cb} = 220$ m. While PBL q_v increased by about 0.5 g kg^{-1} from upwind to the lee of the island, increases in PBL θ appear to be the dominant factor in setting cloud base height.

7 Conclusions

The Southern California Investigation of Low cloud and Land Aerosol (SCILLA) was an airborne field experiment flown in June 2023 off the coast of San Diego, California to sample aerosols, clouds, radiation, trace gases, and meteorology in, below and above planetary boundary layer clouds over the Southern California Bight to explore linkages among these observables. In particular, the measurements are intended to give insight on how shallow mesoscale circulations and the topography of the Channel Islands (more specifically, San Clemente Island) interact with boundary layer flow and modulate exchange between the boundary layer and the lower free troposphere. In this paper we described the sampling strategies employed during research flights; outlined the scientific payload of the aircraft, the in situ measurements available, and auxiliary datasets provided; and gave a detailed overview of flights by mission objective. Forthcoming studies will evaluate the scientific hypotheses motivating SCILLA with more detailed analysis than is possible in this manuscript.

8 Data availability

All data referenced in this paper are freely available for download via the following DOIs/links:

- Merged 1 and 10 Hz aircraft data, https://doi.org/10.5439/2530546, Witte et al. (2025a) or https://doi.org/10.5281/zenodo.21826965, Witte et al. (2026a)
- Mini-aerosol mass spectrometer (mAMS) airborne data, https://doi.org/10.5439/2570854, Bahreini et al. (2025)
- Nitrogen oxides (NOx) airborne data, https://doi.org/10.5439/2572200, Collins et al. (2025a)
- Ozone (O3) airborne data, https://doi.org/10.5439/2572208, Collins et al. (2025b)
- Secondary aerosol volume concentration airborne data, https://doi.org/10.5439/2574044, Collins et al. (2025c)
- Scanning electrical mobility spectrometer (SEMS) airborne data, https://doi.org/10.5439/2588599, Metcalf et al. (2025)
- Combined repository for sub-1 Hz measurements (mAMS, NOx, O3, secondary aerosol concentration, and SEMS): https://doi.org/10.5281/zenodo.22283324, Witte et al. (2026b)
- Flight scientist reports, https://doi.org/10.5281/zenodo.15353160, Witte et al. (2025b)

Video supplement. Forward cockpit video from the aircraft is freely available at https://youtu.be/DilmQmxxuUs?si=mRRHGmn7CD2RP0Mx, (Witte et al., 2025c)

Appendix A: Flight-by-flight instrument status

Instrument status for each SCILLA flight is shown in Table A1.

Author contributions. MKW: conceptualization, data curation, formal analysis, funding acquisition, investigation, methodology, project administration, resources, software, supervision, visualization, writing – original draft, writing – review & editing. RB: data curation, formal

https://doi.org/10.5194/essd-2026-593
Preprint. Discussion started: 4 September 2026

Open Access Earth System Science Data Discussions

Table A1. Flight-by-flight instrument status summary. See legend below for status codes.

Flight Info		Inlets		Aerosol Physics/Chemistry					Optical Particle Counters					Gases/H_2O Isotopes				Facility (MET, NAV, radiation, etc.)						
RF	Date	CVI	Rev. Inlet	AMS*	OFR**	SEMS*	SP2*	TAP*	UFCPC	wCPC*	PCASP	CAPS	PDI	WVIA**	O3**	NOx**	CO2*	MET	NAV	Gerber	LiCor	RAD	SST	Video
2	Jun 6	▽	CL	×	×	✓	✓	×	✓	×	✓	✓	✓	✓	✓	✓	✓	✓	✓	✓	✓	△[a]	✓	✓
3	Jun 9	✓	CL	×	×	✓	✓	✓	×	×	✓	✓	✓	✓	✓	✓	✓	✓	✓	✓	✓	△[a]	✓	✓
4	Jun 10	✓	CL	✓	×	✓	✓	✓	✓	×	✓	✓	✓	✓	✓	✓	✓	✓	✓	✓	✓	✓	✓	✓
5	Jun 11	↔	CL	×	×	✓	✓	✓	✓	✓	✓	✓	✓	✓	✓	✓	✓	△[b]	×[c]	✓	✓	✓	✓	✓
6	Jun 12	↔	CL	×	×	✓	✓	✓	✓	✓	✓	✓	✓	✓	✓	✓	✓	✓	✓	✓	✓	✓	✓	✓
7	Jun 13	✓	CL	✓	×	✓	✓	✓	✓	✓	✓	✓	✓	✓	✓	✓	✓	✓	✓	✓	✓	✓	✓	✓
8	Jun 15	↔	CL	×	×	✓	✓	✓	✓	×	✓	✓	✓	✓	✓	✓	✓	✓	✓	✓	✓	✓	✓	✓
9	Jun 16	×	✓	✓	△	✓	✓	✓	✓	✓	✓	✓	×	✓	✓	✓	✓	✓	✓	✓	✓	✓	✓	✓
10	Jun 19	✓	✓	✓	△	✓	✓	✓	✓	✓	✓	✓	✓	×	✓	✓	✓	✓	✓	✓	✓	✓	✓	✓
11	Jun 20	×	✓	✓	▽	✓	✓	✓	✓	✓	✓	✓	×	✓	×	✓	✓	✓	✓	✓	✓	✓	✓	✓
12	Jun 21	×	✓	×	△	✓	✓	✓	✓	✓	✓	✓	×	✓	✓	✓	✓	✓	✓	✓	✓	✓	✓	✓
13	Jun 22	✓	✓	✓	✓	✓	✓	✓	✓	✓	✓	✓	✓	✓	×	✓	✓	✓	✓	✓	✓	✓	✓	✓
14	Jun 23	✓	LW?	×	✓	✓	✓	✓	✓	✓	✓	✓	△[d]	△	✓	✓	✓	✓	✓	✓	✓	✓	✓	✓
15	Jun 24	✓	LW?	✓	✓	✓	✓	✓	✓	✓	✓	✓	✓	△	✓	✓	✓	✓	✓	✓	✓	✓	✓	✓
16	Jun 26	✓	LW?	✓	✓	✓	✓	✓	✓	✓	✓	✓	✓	△	✓	✓	✓	✓	✓	×[c]	✓	✓	✓	✓
17	Jun 27	✓	LW?	✓	✓	✓	✓	✓	✓	✓	✓	✓	✓	△	✓	✓	✓	✓	✓	✓	✓	✓	✓	✓
18	Jun 28	✓	✓	✓	✓	✓	✓	✓	✓	✓	✓	✓	✓	✓	✓	✓	✓	✓	✓	✓	✓	✓	✓	✓
19	Jun 29	✓	LW?	✓	✓	✓	✓	✓	✓	✓	✓	✓	✓	△	✓	✓	✓	✓	✓	✓	✓	✓	✓	✓
20	Jun 29	✓	✓	✓	✓	✓	✓	✓	✓	✓	✓	✓	×	✓	✓	✓	✓	✓	✓	✓	✓	✓	✓	✓
21	Jun 30	✓	✓	✓	✓	✓	✓	✓	✓	✓	✓	✓	✓	✓	✓	✓	✓	✓	✓	✓	✓	✓	✓	✓

Status codes: ✓ OK   △ functioning >50% of flight   ▽ functioning <50% of flight   × down / no usable data

Inlet-specific codes: ↔ CVI flow reversed   CL cabin leak (reverse inlet)   LW? liquid water suspected (reverse inlet)

* behind CVI inlet   ** behind reverse inlet

Notes:

[a] RF1, RF2 – RAD: CM22 nadir solar channel inoperative.

[b] RF5 – MET: dew point sensor exceeded range on descents below ~1000 ft.

[c] RF5, RF16 – NAV: C-MIGITS unit down.

[d] RF14 – PDI: missing data on second module cloud base leg.

analysis, investigation, methodology, project administration, resources, supervision, writing – original draft, writing – original draft. SB: formal analysis, investigation. AB: data curation, formal analysis, investigation, methodology, project administration, resources, supervision. PYC: conceptualization, formal analysis, funding acquisition, investigation, methodology, project administration, resources, supervision, writing – original draft, writing – review & editing. DC: data curation, formal analysis, funding acquisition, investigation, methodology, project administration, resources, supervision, writing – review & editing. MH: data curation, formal analysis, investigation, resources, writing – original draft. MDL: data curation, formal analysis, investigation, resources, writing – original draft. ABM: investigation, methodology. ARM: data curation, formal analysis, investigation, methodology, resources, supervision, writing – review & editing. BR: data curation, formal analysis, investigation, resources, writing – original draft. NS: data curation, formal analysis. DW: data curation, formal analysis, investigation, resources, writing – original draft. LRW: data curation, formal analysis, funding acquisition, investigation, methodology, resources, supervision, writing – original draft, writing – original draft.

Competing interests. The authors declare no competing interests.

Disclaimer. The opinions and views expressed are those of the author alone and do not necessarily represent those of the U.S. Government, U.S. Department of War or its components, to include the Department of the Navy and the Naval Postgraduate School.

Acknowledgements. The authors thank the pilots and crew of the CIRPAS Twin Otter for their dedication and professionalism: Greg Cooper, Bryce Kujat, Jeff Martin, and Roy Woods. This type of fieldwork is not possible without the knowledge, passion and tireless work ethic of these critical team members. We also thank FACSFAC-SD and specifically Mr. Loren Brown for working with the science team to understand our sampling goals and help schedule flights in an extremely busy airspace, and Prof. Christopher Post (Clemson University) for use of the LI-COR CO_2 gas analyzer. MKW acknowledges support from the Office of Naval Research Marine Meteorology program under funding documents N0001422WX02037, N0001423WX00321, N0001424WX00987, N0001424WX02097, and O2502017017085289. This work was also supported by the U.S. Department of Energy's Atmospheric System Research, an Office of Science Biological and Environmental Research program, under Grant No. DE-SC0023054 (DC, RB, ARM) and DE-SC0024104 (LRW and PYC).

References

Allan, J. D., Delia, A. E., Coe, H., Bower, K. N., Alfarra, M., Jimenez, J. L., Middlebrook, A. M., Drewnick, F., Onasch, T. B., Canagaratna, M. R., Jayne, J. T., and Worsnop, D. R.: A generalised method for the extraction of chemically resolved mass spectra from Aerodyne aerosol mass spectrometer data, Journal of Aerosol Science, 35, 909–922, https://doi.org/https://doi.org/10.1016/j.jaerosci.2004.02.007, 2004.

Bahreini, R., Dunlea, E. J., Matthew, B. M., Simons, C., Docherty, K. S., DeCarlo, P. F., Jimenez, J. L., Brock, C. A., and Middlebrook, A. M.: Design and Operation of a Pressure-Controlled Inlet for Airborne Sampling with an Aerodynamic Aerosol Lens, Aerosol Science and Technology, 42, 465–471, https://doi.org/10.1080/02786820802178514, 2008.

Bahreini, R., Ries, B., MacDonald, A., Bucholtz, A., Witte, M., and Metcalf, A.: SCILLA mini-aerosol mass spectrometer (mAMS) airborne data, ARM Data Discovery [dataset], https://doi.org/10.5439/2570854, 2025.

Chuang, P. Y., Saw, E. W., Small, J. D., Shaw, R. A., Sipperley, C. M., Payne, G. A., and Bachalo, W. D.: Airborne Phase Doppler Interferometry for Cloud Microphysical Measurements, Aerosol Sci. Technol., 42, 685–703, https://doi.org/10.1080/02786820802232956, 2008.

Collins, D., Han, M., Witte, M., and Bucholtz, A.: SCILLA nitrogen oxides (NOx) airborne data, ARM Data Discovery [dataset], https://doi.org/10.5439/2572200, 2025a.

Collins, D., Han, M., Witte, M., and Bucholtz, A.: SCILLA ozone (O3) airborne data, ARM Data Discovery [dataset], https://doi.org/10.5439/2572208, 2025b.

Collins, D., Han, M., Witte, M., and Bucholtz, A.: SCILLA secondary aerosol volume concentration airborne data, ARM Data Discovery [dataset], https://doi.org/10.5439/2574044, 2025c.

Dingle, J. H., Vu, K., Bahreini, R., Apel, E. C., Campos, T. L., Flocke, F., Fried, A., Herndon, S., Hills, A. J., Hornbrook, R. S., Huey, G., Kaser, L., Montzka, D. D., Nowak, J. B., Reeves, M., Richter, D., Roscioli, J. R., Shertz, S., Stell, M., Tanner, D., Tyndall, G., Walega, J., Weibring, P., and Weinheimer, A.: Aerosol optical extinction during the Front Range Air Pollution and Photochemistry Éxperiment (FRAPPÉ) 2014 summertime field campaign, Colorado, USA, Atmospheric Chemistry and Physics, 16, 11 207–11 217, https://doi.org/10.5194/acp-16-11207-2016, 2016.

Galewsky, J.: Water Vapor Isotopic Composition from the Azores Field Campaign Report, Tech. rep., DOE/SC-ARM-19-02, https://doi.org/10.2172/1572385, 2021.

Gao, R. S., Schwarz, J. P., Kelly, K. K., Fahey, D. W., Watts, L. A., Thompson, T. L., Spackman, J. R., Slowik, J. G., Cross, E. S., Han, J.-H., Davidovits, P., Onasch, T. B., and Worsnop, D. R.: A Novel Method for Estimating Light-Scattering Properties of Soot Aerosols Using a Modified Single-Particle Soot Photometer, Aerosol Science and Technology, 41, 125–135, https://doi.org/10.1080/02786820601118398, 2007.

Jayne, J. T., Leard, D. C., Zhang, X., Davidovits, P., Smith, K. A., Kolb, C. E., and Worsnop, D. R.: Development of an Aerosol Mass Spectrometer for Size and Composition Analysis of Submicron Particles, Aerosol Science and Technology, 33, 49–70, https://doi.org/10.1080/027868200410840, 2000.

Jimenez, J. L., Jayne, J. T., Shi, Q., Kolb, C. E., Worsnop, D. R., Yourshaw, I., Seinfeld, J. H., Flagan, R. C., Zhang, X., Smith, K. A., Morris, J. W., and Davidovits, P.: Ambient aerosol sampling using the Aerodyne Aerosol Mass Spectrometer, Journal of Geophysical Research: Atmospheres, 108, https://doi.org/https://doi.org/10.1029/2001JD001213, 2003.

Laing, J. R., Jaffe, D. A., and Sedlacek, A. J.: Comparison of Filter-based Absorption Measurements of Biomass Burning Aerosol and Background Aerosol at the Mt. Bachelor Observatory, Aerosol and Air Quality Research, 20, 663–679, https://doi.org/10.4209/aaqr.2019.06.0298, 2020.

Marto, J. P., Zhang, J., and Schwab, J. J.: Plume analysis from field evaluations of a portable air quality monitoring system, Journal of the Air & Waste Management Association, 71, 70–80, https://doi.org/10.1080/10962247.2020.1834010, 2021.

Metcalf, A., Wang, D., Collins, D., Bahreini, R., Witte, M., and Bucholtz, A.: SCILLA scanning electrical mobility spectrometer (SEMS) airborne data, ARM Data Discovery [dataset], https://doi.org/10.5439/2588599, 2025.

Nault, B. A., Campuzano-Jost, P., Day, D. A., Schroder, J. C., Anderson, B., Beyersdorf, A. J., Blake, D. R., Brune, W. H., Choi, Y., Corr, C. A., de Gouw, J. A., Dibb, J., DiGangi, J. P., Diskin, G. S., Fried, A., Huey, L. G., Kim, M. J., Knote, C. J., Lamb, K. D., Lee, T., Park, T., Pusede, S. E., Scheuer, E., Thornhill, K. L., Woo, J.-H., and Jimenez, J. L.: Secondary organic aerosol production from local emissions dominates the organic aerosol budget over Seoul, South Korea, during KORUS-AQ, Atmospheric Chemistry and Physics, 18, 17 769–17 800, https://doi.org/10.5194/acp-18-17769-2018, 2018.

Ortega, A. M., Hayes, P. L., Peng, Z., Palm, B. B., Hu, W., Day, D. A., Li, R., Cubison, M. J., Brune, W. H., Graus, M., Warneke, C., Gilman, J. B., Kuster, W. C., de Gouw, J., Gutiérrez-Montes, C., and Jimenez, J. L.: Real-time measurements of secondary organic aerosol formation and aging from ambient air in an oxidation flow reactor in the Los Angeles area, Atmospheric Chemistry and Physics, 16, 7411–7433, https://doi.org/10.5194/acp-16-7411-2016, 2016.

Salmon, O. E., Welp, L. R., Baldwin, M. E., Hajny, K. D., Stirm, B. H., and Shepson, P. B.: Vertical profile observations of water vapor deuterium excess in the lower troposphere, Atmospheric Chemistry and Physics, 19, 11 525–11 543, https://doi.org/10.5194/acp-19-11525-2019, 2019.

Schroder, J. C., Hanna, S. J., Modini, R. L., Corrigan, A. L., Kreidenwies, S. M., Macdonald, A. M., Noone, K. J., Russell, L. M., Leaitch, W. R., and Bertram, A. K.: Size-resolved observations of refractory black carbon particles in cloud droplets at a marine boundary layer site, Atmospheric Chemistry and Physics, 15, 1367–1383, https://doi.org/10.5194/acp-15-1367-2015, 2015.

Sorooshian, A., MacDonald, A. B., Dadashazar, H., Bates, K. H., Coggon, M. M., Craven, J. S., Crosbie, E., Hersey, S. P., Hodas, N., Lin, J. J., Negrón Marty, A., Maudlin, L. C., Metcalf, A. R., Murphy, S. M., Padró, L. T., Prabhakar, G., Rissman, T. A., Shingler, T., Varutbangkul, V., Wang, Z., Woods, R. K., Chuang, P. Y., Nenes, A., Jonsson, H. H., Flagan, R. C., and Seinfeld, J. H.: A multi-year data set on aerosol-cloud-precipitation-meteorology interactions for marine stratocumulus clouds, Scientific Data, 5, 180 026, https://doi.org/10.1038/sdata.2018.26, 2018.

Strapp, J. W., Albers, F., Reuter, A., Korolev, A. V., Maixner, U., Rashke, E., and Vukovic, Z.: Laboratory Measurement of the Response of a PMS OAP-2DC, J. Atmos. Oceanic Technol., 18, 1150–1170, 2001.

Sturm, P. and Knohl, A.: Water vapor δ^2H and δ^{18}O measurements using off-axis integrated cavity output spectroscopy, Atmospheric Measurement Techniques, 3, 67–77, https://doi.org/10.5194/amt-3-67-2010, 2010.

Subramanian, R., Kok, G. L., Baumgardner, D., Clarke, A., Shinozuka, Y., Campos, T. L., Heizer, C. G., Stephens, B. B., de Foy, B., Voss, P. B., and Zaveri, R. A.: Black carbon over Mexico: the effect of atmospheric transport on mixing state, mass absorption cross-section, and BC/CO ratios, Atmospheric Chemistry and Physics, 10, 219–237, https://doi.org/10.5194/acp-10-219-2010, 2010.

Vu, K. T., Dingle, J. H., Bahreini, R., Reddy, P. J., Apel, E. C., Campos, T. L., DiGangi, J. P., Diskin, G. S., Fried, A., Herndon, S. C., Hills, A. J., Hornbrook, R. S., Huey, G., Kaser, L., Montzka, D. D., Nowak, J. B., Pusede, S. E., Richter, D., Roscioli, J. R., Sachse, G. W., Shertz, S., Stell, M., Tanner, D., Tyndall, G. S., Walega, J., Weibring, P., Weinheimer, A. J., Pfister, G., and Flocke, F.: Impacts

https://doi.org/10.5194/essd-2026-593
Preprint. Discussion started: 4 September 2026

Open Access Earth System Science Data Discussions

of the Denver Cyclone on regional air quality and aerosol formation in the Colorado Front Range during FRAPPÉ 2014, Atmospheric Chemistry and Physics, 16, 12 039–12 058, https://doi.org/10.5194/acp-16-12039-2016, 2016.

Wakimoto, R. M.: The Catalina Eddy and its Effect on Pollution over Southern California, Monthly Weather Review, 115, 837 – 855, https://doi.org/10.1175/1520-0493(1987)115<0837:TCEAIE>2.0.CO;2, 1987.

Wendisch, M., Garrett, T. J., and Strapp, J. W.: Wind Tunnel Tests of the Airborne PVM-100A Response to Large Droplets, Journal of Atmospheric and Oceanic Technology, 19, 1577 – 1584, https://doi.org/10.1175/1520-0426(2002)019<1577:WTTOTA>2.0.CO;2, 2002.

Witte, M. K., Yuan, T., Chuang, P. Y., Platnick, S., Meyer, K. G., Wind, G., and Jonsson, H. H.: MODIS Retrievals of Cloud Effective Radius in Marine Stratocumulus Exhibit No Significant Bias, Geophysical Research Letters, 45, 10,656–10,664, https://doi.org/10.1029/2018GL079325, 2018.

Witte, M. K., Bahreini, R., Chuang, P., Collins, D., Han, M., Leandro, M., Metcalf, A., Ries, B., Wang, D., Welp, L., and Bucholtz, A.: SCILLA merged 1 Hz and 10 Hz airborne data, ARM Data Discvovery [dataset], https://doi.org/10.5439/2530546, 2025a.

Witte, M. K., Chuang, P. Y., and Leandro, M.: Flight scientist reports from the Southern California Investigation of Low cloud and Land Aerosol (SCILLA), https://doi.org/10.5281/zenodo.15353160, 2025b.

Witte, M. K., Woods, R., and Bucholtz, A.: SCILLA forward cockpit video, https://youtu.be/DilmQmxxuUs?si=mRRHGmn7CD2RP0Mx, (Last accessed 24 July 2026), 2025c.

Witte, M. K., Bahreini, R., Chuang, P., Collins, D., Han, M., Leandro, M., Metcalf, A., Ries, B., Wang, D., Welp, L., and Bucholtz, A.: SCILLA merged 1 Hz and 10 Hz airborne data, Zenodo [dataset], https://doi.org/https://doi.org/10.5281/zenodo.21826965, 2026a.

Witte, M. K., Bahreini, R., Collins, D., Han, M., MacDonald, A., Metcalf, A., Ries, B., Wang, D., and Bucholtz, A.: SCILLA sub-1 Hz Data, Zenodo [dataset], https://doi.org/https://doi.org/10.5281/zenodo.22283324, 2026b.

Wolfe, G.: Flux Toolbox GitHub repository, https://github.com/AirChem/FluxToolbox, (Last accessed 24 July 2026), 2025.

Xu, N., Le, C., Cocker, D. R., Chen, K., Lin, Y.-H., and Collins, D. R.: An oxidation flow reactor for simulating and accelerating secondary aerosol formation in aerosol liquid water and cloud droplets, Atmospheric Measurement Techniques, 17, 4227–4243, https://doi.org/10.5194/amt-17-4227-2024, 2024.